Since January 2020 Elsevier has created a COVID-19 resource centre with free information in English and Mandarin on the novel coronavirus COVID-19. The COVID-19 resource centre is hosted on Elsevier Connect, the company's public news and information website.

Redox Biology 58 (2022) 102508

Contents lists available at ScienceDirect

Redox Biology

journal homepage: www.elsevier.com/locate/redox

SARS-CoV-2 mitochondriopathy in COVID-19 pneumonia exacerbates hypoxemia

Stephen L. Archer [a,b,*], Asish Dasgupta [a], Kuang-Hueih Chen [a], Danchen Wu [a], Kaushal Baid [c], John E. Mamatis [d], Victoria Gonzalez [c,e], Austin Read [a], Rachel ET. Bentley [a], Ashley Y. Martin [a], Jeffrey D. Mewburn [a], Kimberly J. Dunham-Snary [a,d], Gerald A. Evans [a], Gary Levy [f], Oliver Jones [b], Ruaa Al-Qazazi [a], Brooke Ring [b], Elahe Alizadeh [b], Charles CT. Hindmarch [b], Jenna Rossi [a], Patricia DA. Lima [b], Darryl Falzarano [c,e], Arinjay Banerjee [c,e,g,h], Che C. Colpitts [d]

[a] Department of Medicine, Queen's University, Kingston, ON, Canada
[b] Queen's Cardiopulmonary Unit (QCPU), Queen's University, Kingston, ON, Canada
[c] Vaccine and Infectious Disease Organization, University of Saskatchewan, Saskatoon, SK, Canada
[d] Department of Biomedical and Molecular Sciences, Queen's University, Kingston, ON, Canada
[e] Department of Veterinary Microbiology, Western College of Veterinary Medicine, University of Saskatchewan; Saskatoon, SK, Canada
[f] University of Toronto, Toronto, ON, Canada
[g] Department of Laboratory Medicine and Pathobiology, University of Toronto, Toronto, ON, Canada
[h] Department of Biology, University of Waterloo; Waterloo, ON, Canada

ARTICLE INFO

Keywords:
Apoptosis
Hypoxic pulmonary vasoconstriction
HCoV-OC43
Murine hepatitis virus (MHV-1)
Apoptosis inducing factor (AIF)
Dynamin related protein 1 (Drp1)
Mitochondrial fission
Mitochondrial permeability transition pore (mPTP)

ABSTRACT

Rationale: Severe acute respiratory syndrome coronavirus 2 (SARS-CoV-2) causes COVID-19 pneumonia. We hypothesize that SARS-CoV-2 causes alveolar injury and hypoxemia by damaging mitochondria in airway epithelial cells (AEC) and pulmonary artery smooth muscle cells (PASMC), triggering apoptosis and bioenergetic impairment, and impairing hypoxic pulmonary vasoconstriction (HPV), respectively.
Objectives: We examined the effects of: A) human betacoronaviruses, SARS-CoV-2 and HCoV-OC43, and individual SARS-CoV-2 proteins on apoptosis, mitochondrial fission, and bioenergetics in AEC; and B) SARS-CoV-2 proteins and mouse hepatitis virus (MHV-1) infection on HPV.
Methods: We used transcriptomic data to identify temporal changes in mitochondrial-relevant gene ontology (GO) pathways post-SARS-CoV-2 infection. We also transduced AECs with SARS-CoV-2 proteins (M, Nsp7 or Nsp9) and determined effects on mitochondrial permeability transition pore (mPTP) activity, relative membrane potential, apoptosis, mitochondrial fission, and oxygen consumption rates (OCR). In human PASMC, we assessed the effects of SARS-CoV-2 proteins on hypoxic increases in cytosolic calcium, an HPV proxy. In MHV-1 pneumonia, we assessed HPV via cardiac catheterization and apoptosis using the TUNEL assay.
Results: SARS-CoV-2 regulated *mitochondrial apoptosis, mitochondrial membrane permeabilization* and *electron transport chain (ETC)* GO pathways within 2 hours of infection. SARS-CoV-2 downregulated ETC Complex I and ATP synthase genes, and upregulated apoptosis-inducing genes. SARS-CoV-2 and HCoV-OC43 upregulated and activated dynamin-related protein 1 (Drp1) and increased mitochondrial fission. SARS-CoV-2 and transduced SARS-CoV-2 proteins increased apoptosis inducing factor (AIF) expression and activated caspase 7, resulting in apoptosis. Coronaviruses also reduced OCR, decreased ETC Complex I activity and lowered ATP levels in AEC. M protein transduction also increased mPTP opening. In human PASMC, M and Nsp9 proteins inhibited HPV. In MHV-1 pneumonia, infected AEC displayed apoptosis and HPV was suppressed. BAY K8644, a calcium channel agonist, increased HPV and improved SpO_2.
Conclusions: Coronaviruses, including SARS-CoV-2, cause AEC apoptosis, mitochondrial fission, and bioenergetic impairment. SARS-CoV-2 also suppresses HPV by targeting mitochondria. This mitochondriopathy is replicated by transduction with SARS-CoV-2 proteins, indicating a mechanistic role for viral-host mitochondrial protein

* Corresponding author. Head Department of Medicine, Queen's University Etherington Hall, Room 3041 94 Stuart St., Kingston, Ontario, K7L 3N6, Canada.
E-mail address: stephen.archer@queensu.ca (S.L. Archer).

https://doi.org/10.1016/j.redox.2022.102508
Received 27 September 2022; Accepted 9 October 2022
Available online 13 October 2022

interactions. Mitochondriopathy is a conserved feature of coronaviral pneumonia that may exacerbate hypoxemia and constitutes a therapeutic target.

1. Introduction

COVID-19 pneumonia is an acute respiratory illness caused by the novel betacoronavirus, SARS-CoV-2, an enveloped, single-stranded, positive-sense, RNA virus. By mid-September 2022, the COVID-19 pandemic had caused >614 million infections, >6.5 million deaths, and global trade disruption. While most infected people are paucisymptomatic, ~5% suffer respiratory failure requiring hospitalization [1] and in Canada ~1.1% of infected patients have died [2]. Patients with severe COVID-19 pneumonia suffer from diffuse alveolar damage (DAD), and hypoxemia. While COVID-19 pneumonia has features of acute respiratory distress syndrome (ARDS), including DAD, microthrombi, inflammation and alveolar edema [3], the lungs of COVID-19 patients are less stiff, and their hypoxemia is in part related to ventilation/perfusion (V/Q) mismatch [4]. In early 2020 we proposed that SARS-CoV-2 caused hypoxia in COVID-19 pneumonia by causing malfunction of oxygen-sensing mechanisms, including loss of HPV, and by triggering mitochondrial-induced apoptosis of lung airway epithelial cells (AEC) [5].

Mitochondria are organelles that mediate apoptosis [6], serve as oxygen-sensors [7] and are known viral targets. Many viruses, including SARS-CoV [8,9], cause apoptosis by targeting mitochondria [10,11]. Therefore, we hypothesized that lung injury and hypoxemia in COVID-19 result, in part, from coronavirus-induced mitochondrial damage in i) AEC, resulting in DAD, and ii) pulmonary artery smooth muscle cells (PASMC), impairing hypoxic pulmonary vasoconstriction (HPV) thereby increasing V/Q mismatch [5].

Viruses may cause apoptosis by stimulating transcription of homologs that mimic the host's apoptosis proteins and/or by transduction with viral proteins that interact with host proteins which regulate apoptosis [12]. For example, viral-mitochondrial protein interactions can open the mitochondrial permeability transition pore (mPTP) [13], which depolarizes mitochondrial membrane potential ($\Delta\Psi m$). mPTP opening and $\Delta\Psi m$ depolarization cause BH3-interacting domain death agonist (Bid) to permeabilize the mitochondrial membrane, releasing apoptosis inducing factor (AIF) and cytochrome *c* from the mitochondrial intermembrane space [14]. Once released, cytosolic AIF and cytochrome *c* activate caspases and enter the nucleus, promoting DNA degradation, resulting in apoptotic cell death [15]. Lai et al. showed that SARS-CoV, the coronavirus which caused SARS, alters the expression of numerous mitochondrial proteins involved in mitochondrial electron transport chain (ETC) function and apoptosis [16].

Less is known about the effects of SARS-CoV-2 on mitochondria. SARS-CoV-2's 30 kb genome encodes 16 non-structural proteins (Nsp) that form a replicase/transcriptase complex, four structural proteins, and nine accessory factors. Gordon et al. identified 332 SARS-CoV-2–host protein interactions, several of which are predicted to involve mitochondrial proteins, which could impair O_2-sensing and/or trigger apoptosis [17]. Most of these SARS-CoV-2 protein interactions occurred with proteins expressed in the lung and included many proteins in the mitochondrial matrix [17]. SARS-CoV-2 proteins (Nsp4, Nsp7, Nsp8, Orf9c and M) interact with mitochondrial targets, including metabolic factors, mitochondrial ribosomal targets, and subunits of ETC Complex I [17]. Nsp5, SARS-CoV-2's main protease, may interfere with protein transport into the endoplasmic reticulum and mitochondria. Nsp7 interacts with host mitochondrial proteins NDUFAF1 and NDUFAF2 [17], which are involved in ETC Complex I assembly. ETC Complex I is potentially important to COVID-19-related hypoxemia because it is the location of the PASMC's O_2-sensor [18]. Although Gordon [17] identified protein-protein interactions between SARS-CoV-2 and mitochondria, the occurrence of these interactions *in vivo* and their functional consequences were not studied.

To determine the mechanism of COVID-19 induced mitochondriopathy, we studied two replicating human betacoronaviruses, SARS-CoV-2 and HCoV-OC43, as well as a murine coronavirus (MHV-1). We also studied the effects of lentivirally-mediated expression of individual SARS-CoV-2 proteins (M, Nsp7, and Nsp9) that were selected because they have a mitochondrial interactome [17]. We show that replicating coronaviruses target mitochondria, impairing mitochondrial bioenergetics, triggering mitochondrial fission and inducing AEC apoptosis. Within hours of infection, numerous mitochondrial gene ontology (GO) pathways affecting mitochondrial membrane permeability, bioenergetics, electron transport, ATP synthesis and mitochondrial fission are regulated. These findings are recapitulated by infection with HCoV-OC43, a pathogenic betacoronavirus that causes lower respiratory tract infections in humans [19–21], and are also reproduced by heterologous expression of SARS-CoV-2 proteins. This study shows that SARS-CoV-2 causes AEC apoptosis, which contributes to airway injury in coronavirus pneumonia. We also show for the first time that transduction with SARS-CoV-2 proteins or MHV-1 infection suppresses HPV and that conversely, enhancing HPV increases systemic oxygenation in a coronavirus pneumonia model. We describe a mitochondriopathy that is induced by SARS-CoV-2 and is a conserved feature of infection with other betacoronaviruses.

2. Methods

Ethics approval

Infection with SARS-CoV-2 was performed at the CL3 laboratory at Vaccine and Infectious Disease Organization (VIDO), University of Saskatchewan, following their approved protocols. All other experiments were performed at Queen's University, following protocols in TRAQ 6028150 and TRAQ 6020690. Experiments using animals were conducted with careful attention to ethical animal handling, as approved by the Queen's University Animal Care Committee.

2.1. Statistics and experimental design

All experiments were randomized, and scientists were blinded to treatment group, following best experimental practices [22]. Sample size was ≥5 for each experiment, unless otherwise stated. Normality of data was tested, and all normally distributed data were expressed as mean ± SEM. Statistical analysis was performed using Students t-test or ANOVA, as appropriate. A p-value <0.05, corrected for multiple comparisons or evaluated by Tukey's test, was considered statistically significant. Sample size for the MHV-1 pneumonia model was chosen as $> n = 9$/group, based on a power calculation informed by pilot studies to ensure 80% power to detect a significant MHV-1 effect on systemic oxygenation with a $p<0.05$. Both sexes were used in the MHV-1 pneumonia model; results were similar between sexes, so data were analyzed in aggregate.

2.2. Approach

To understand how coronaviruses affect human and murine AEC, human pulmonary artery smooth muscle cells (PASMC) and human PA endothelial cells (HPAEC) we studied the effects of three replicating coronaviruses including two human pathogens, SARS-CoV-2 and HCoV-OC43, and a murine subgroup 2a betacoronavirus, MHV-1. To understand mechanisms of mitochondrial injury we also studied the effects of transduction of AEC and PASMC with individual SARS-CoV-2 proteins.

Our strategy of using multiple coronaviruses was both strategic (to examine the degree to which mitochondrial damage was a conserved mechanism of cell injury) and practical (some mechanistic and physiological experiments were logistically difficult to perform within the CL3 laboratory conditions required to study replicating SARS-CoV-2).

SARS-CoV-2 was studied in Calu-3 cells (human lung adenocarcinoma derived AEC). In these experiments we measured the effect of infection on the transcriptome, assessed mitochondrial dynamics and confirmed the occurrence of Drp1-mediated mitochondrial fission and activation of mitochondrial apoptosis pathways. We also studied individual SARS-CoV-2 proteins that interact with human mitochondrial proteins by transducing BEAS-2B cells (human bronchial AEC immortalized using a SV40/adenovirus) using lentiviral vectors [17]. In BEAS-2B cells, we measured the effects of SARS-CoV-2 proteins on mitochondrial transition pore (mPTP) activity, mitochondrial membrane potential ($\Delta\Psi m$), apoptosis, mitochondrial dynamics, cell cycle regulation and oxidative glucose metabolism, including ETC Complex I activity. We confirmed the efficacy of these lentiviral vectors to achieve transduction using human non-small cell lung cancer cells (A549 cells), a cell line selected for this limited use because of their rapid growth rate. We also studied the effects of infection with the human betacoronavirus, HCoV-OC43 in BEAS-2B cells, measuring effects on mitochondrial membrane potential, apoptosis, bioenergetics (Complex I activity and ATP concentrations) and mitochondrial dynamics. HCoV-OC43 infection was also studied in normal non-transformed human pulmonary artery endothelial cells (HPAEC).

To study the effects of coronaviruses on HPV we transduced non-transformed, normal, human PASMC with SARS-CoV-2 proteins. We assessed the effects of viral proteins on the rise in intracellular calcium, $[Ca^{2+}]_i$. elicited by acute hypoxia, as a surrogate for HPV. We also used the MHV-1 pneumonia model to study HPV *in vivo* in infected mice. When injected into the nares of A/J mice, MHV-1 creates a model that reflects key aspects of COVID-19 pneumonia, creating infiltrates and hypoxemia [23,24]. MHV-1 was also studied in murine adenoma cells (LA-4 cells). In these experiments we measured mitochondrial membrane potential and apoptosis.

2.3. Cell culture

Calu-3 AEC (American Type Culture Collection, ATCC, (Manassas, VA, USA) were cultured as previously described [25]. Human non-neoplastic bronchial epithelial cells, BEAS-2B, were purchased from ATCC and cultured in bronchial epithelial cell growth medium (Lonza/Clonetics Corporation, Basel, Switzerland), following ATCC instructions. LA-4 adenoma cells were cultured in F–12K medium (Gibco, Waltham, MA, USA) supplemented with 15% FBS. A549 cells (ATCC) were maintained in Dulbecco's Modified Eagle Medium (Sigma-Aldrich, St. Louis, MO, USA) supplemented with 10% FBS. PASMC were grown in Medium 231 supplemented with smooth muscle growth supplement (Life Technologies, Carlsbad, CA, USA). HPAEC (Lonza) were purchased and cultured in endothelial growth medium (EGM)-2 supplemented with the EGM-2 Bullet Kit (Lonza).

2.4. Viral infection

2.4.1. SARS-CoV-2

SARS-CoV-2 experiments were conducted using human Calu-3 cells. A low multiplicity of infection (MOI, 0.01) of wildtype SARS-CoV-2 was used, as previously described [25,26]. Infection was confirmed by detecting infectious virus production (TCID50 assay), qRT-PCR to detect viral genome copies and immunoblot analysis using a SARS-CoV-2 nucleocapsid protein antibody [26]. Experiments were performed 1–72 hours post-infection.

2.4.2. HCoV-OC43

HCoV-OC43 infection was performed in BEAS-2B and HPAEC. Cells were infected for 2 hours in serum-free media (MOI, 3 focus-forming units (ffu)/cell), then inoculum was replaced with complete growth medium and incubated at 33 °C until 48–72 hours post-infection (the time of the experimental endpoint). Infection was confirmed using the antibody against HCoV-OC43 strain, clone 541, N protein (MAB9012, Millipore, Burlington, MA, USA).

2.4.3. MHV-1 amplification and titration

MHV-1 amplification was performed in 17CL-1 cells. Viral titration and expansion were performed in L929 cells using a standard plaque assay. Viral titer was expressed in plaque forming units (PFU). Briefly, MHV-1 was serially diluted and cells were inoculated and incubated at 37 °C for 1 hour allowing viral adsorption. Cells were then overlaid with DMEM containing 1.2% carboxymethylcellulose and 2% FBS and incubated at 37 °C in 5% CO_2 for 36–40 hours. To calculate PFU, cultures were then fixed with formaldehyde and stained with crystal violet. 17CL-1 cells, L929 cells and MHV-1 viral stock were a gift from Dr. Gary Levy (University of Toronto).

2.4.4. Lentivirus packaging and titration

Lentiviral vectors were created for transient transduction of Nsp7, Nsp9, and M SARS-CoV-2 proteins and a Lenti-GFP control (gifts from Dr. Nevan Krogan) [17]. 293T cells were seeded and transfected with the envelope plasmid (pCMV-VSV-G), packaging plasmid (psPAX2) and a transfer plasmid carrying one of the COVID-19 protein genes. Lentiviral plasmids were obtained from Addgene, including: pCMV-VSV-G (Addgene #8454) and the psPAX2 lentiviral packaging plasmid (Addgene #12260). Lentiviruses were collected 48–96 hours after transfection. Lentivirus titration was performed using a One-Wash™ Lentivirus Titer kit HIV-1 p24 Elisa Assay (OriGene, Rockville, MD, USA), per manufacturer's protocol. Cells were transduced with lentiviruses carrying the indicated SARS-CoV-2 gene constructs at 1000 lentiviral particles/cell. Transient transduction was enhanced using polybrene (Millipore). Candidate proteins (Nsp7, Nsp9, and M) were chosen based on the published SARS-CoV-2 human lung interactome [17], which identified each of these proteins as interacting with multiple human mitochondrial proteins.

2.4.5. Transcriptomics

RNA sequencing data were generated from human airway epithelial cells (Calu-3) infected with a clinical isolate of SARS-CoV-2 [27] or mock infected, using a control group exposed to identical media conditions. Both infected and mock infected cells were harvested at 0, 1, 2, 3, 6 or 12 hours post infection [26]. Raw Salmon count files, kindly provided by the authors, were remined to establish the specific effects of SARS-CoV-2 infection on genes that participate in mitochondrial functions. We reanalyzed these data within the R environment and applied DESeq2 [28] to establish differentially regulated genes between infection and mock vehicle control at each time point (e.g. infection vs. mock at $t = n$). In order to understand the functional groups enriched within these lists, we used ClusterProfiler [29] to establish the statistically significant Gene Ontology (GO) pathways at each of the 5 time points. We then filtered these lists as required using wildcard operators, such as "mito" to or "apop", to capture specific pathways of interest. Data are presented using dotplots, CNET diagrams and heatmaps generated using ClusterProfiler or path tools in the R environment. We confirmed our transcriptomic data by measuring the effects of infection on several regulated mitochondrial-relevant transcripts at the protein level using immunoblotting. Specifically, we showed upregulation of the activated form of the mitochondrial fission mediator Drp1, confirmed the upregulation of apoptosis mediators (increased expression of apoptosis inducing factor, AIF) and demonstrated activation of apoptosis (increased expression of cleaved caspase 7).

2.5. Immunoblotting and antibodies

2.5.1. SARS-CoV-2 infected Calu3 AEC (immunoblotting)

Whole-cell lysates were inactivated with sodium dodecyl sulfate (SDS) and heat and transferred from VIDO to Queen's University. They were then prepared with cell lysis buffer (Cell Signaling Technologies, Beverly MA, USA). Cell lysates (40–60 μg) were analyzed for immunoblot analyses on 4–12% NuPAGE gels (Life Technologies, Carlsbad, CA, USA). The proteins were electrotransferred to a polyvinylidene difluoride (PVDF) membrane (Life Technologies, Carlsbad, CA, USA) and detected using the indicated antibodies and ECL-Plus Western Blotting Detection System (GE Healthcare, Piscataway, NJ, USA). Antibodies against cleaved caspase 7 (9491), caspase 7 (12827), SARS-CoV-2 N-protein (33717), AIF (5318), p-Drp1 (ser616) (3455), Smac/DIABLO (15108), Caspase 1(2225) and Bid (2002) were purchased from Cell Signaling Technology (Beverly, MA, USA). Total Drp1antibody (611112) was obtained from BD Transduction Laboratories (San Jose, CA, USA). OC43 N-protein (MAB 9012) was purchased from (Millipore, Burlington, MA, USA). CDK4 (11026-1-AP) and Fis1 (10956-1-AP) antibodies were obtained from Proteintech (Tucson, AZ, USA). Streptavidin antibody (MA5-17283) was purchased from Invitrogen (Waltham, MA, USA). β-actin antibody (A5441) was obtained from Sigma-Aldrich (St. Louis, MO, USA).

2.5.2. SARS-CoV-2 infected Calu-3 AEC (immunofluorescence)

To localize and semi-quantitatively measure expression of mitochondrial proteins of interest we performed immunofluorescent confocal microscopy of Calu-3 AEC infected with SARS-CoV-2. Thermofisher chamber slides containing Mock and SARS-CoV-2 infected Calu-3 cells were transferred from VIDO to Queen's University. Individual chambers were permeabilized with Triton-X 0.2% for 10 minutes and washed. The slides were then incubated with antibodies against p-$Drp1_{S616}$ (1:200 Cell signaling technology), Drp1 (1:400 BD transduction Laboratories) and Tomm20 (1:1000 BD Biosciences) for 1 hour at room temperature. After 3 washes, secondary antibodies conjugated with Alexa-fluor 488 (1:400 Life Technologies) and Alexa-fluor 546 (1:400 Life technologies) were added and incubated for 60 minutes. Slides were washed, a cover slip was applied, and imaging was performed. We recorded 5 fields of view with 6–8 cells per field, using a Leica SP8 confocal microscope. Mean fluorescent intensities in arbitrary units (A.U.) were measured for each field.

2.5.3. SARS-CoV-2 proteins transduced BEAS-2B cells

BEAS-2B cells were grown on 25 mm coverslips and transduced with SARS-CoV-2 proteins for 72–96 hours or infected with HCoV-OC43 (0.05 pfu/cell) for 72 hours. Cells were stained with Mito Tracker™ Deep Red (150 nM, Thermo Fisher Scientific, Waltham, MA, USA) and incubated overnight with AIF (1:200) and TOMM20 (1:1000) primary antibodies and goat anti-Mouse IgG Alexa Fluor Plus 488 or Alexa Fluor 546 goat anti-rabbit secondary antibodies, respectively (Thermofisher, A11035). SOD2 (1:500, #66474-1-Ig, Proteintech) was also used to image mitochondria in BEAS-2B cells infected with HCoV-OC43. Coverslips were mounted with Prolong Diamond Anti-Fade with DAPI and imaged at excitation/emission: 491nm/515–535, using a Leica SP8 confocal microscope and a 63 × 1.4 NA objective. The images were analyzed by ImageJ.

2.5.4. MHV-1 infected murine LA-4 cells

Murine LA-4 cells were infected with MHV-1 and AIF was imaged using the same methods used for BEAS-2B cells.

2.5.5. HCoV-OC43 infected BEAS-2B cells

Expression of apoptosis mediators, mitochondrial fission mediators, and cell cycle regulators were quantified using immunoblotting 72 hours post-infection in BEAS-2B cells infected with HCoV-OC43 [18]. The following antibodies were used: Cell Signaling Technologies (Beverly, MA, USA) - Bid (2002S), AIF (1D39D2), Smac/DIABLO (D5S3R), and Caspase 1 (2225S), phospho-DRP serine 616 (3455S); cyclin dependent kinase 4, CDK4 (110026-1-AP, Proteintech, Tucson, AZ, USA).

2.6. Assessment of apoptosis

2.6.1. In SARS-CoV-2 infected Calu-3 cells

In these infected cells we used immunoblots to measure expression of AIF and both total and cleaved caspase 7, a key mediator in the mitochondrial apoptosis pathway.

2.6.2. In A549 and BEAS-2B AEC

Apoptosis was quantified using the Alexa-fluor 488 Annexin V/Dead Cell Apoptosis Kit (Life Technologies, Carlsbad, CA, USA) using a flow cytometer (SH–800S Sony, Sony Biotechnology Inc, CA. USA). Apoptotic cells were defined as those that were Annexin V^+ and propidium iodide $(PI)^-$. All apoptosis assays were performed 96 hours post-transduction, following the manufacturer's protocols.

2.6.3. In MHV-1 infected mice

Apoptosis was measured in mice with MHV-1 pneumonia using a TUNEL immunofluorescence assay. Lungs were harvested from control and MHV-1 infected mice, formalin-fixed, paraffin-embedded, sectioned and then dual stained with Click-iT® Plus TUNEL (Thermofisher) and 4′,6-diamidino-2-phenylindole (DAPI). To confirm MHV-1 infection, the same sections were blocked with 3% BSA in PBS at 37 °C for 1 hour and an MHV A59 Nsp9 antibody (NBP-21671, Novus Biologicals, Centennial, CO, USA) was applied (1:500 for 1 hour at 37 °C). Finally an Alexa Fluor 546 goat anti-mouse secondary antibody (Thermofisher, A11035) was applied at 1:400 and the slides were incubated for 1 hour at 37 °C. Images were then captured on a Leica SP8 confocal microscope using a 63X 1.4 NA objective and a white light laser at 488 nm. Emission acquisition gating was 510–530 nm (for TUNEL). A 405 nm laser diode was used for DAPI excitation and the emission acquisition gate was set at 420–480 nm. Images were captured using the tile scan function in LAS X software to acquire a total of 9 tiles per tissue slice in a 4-slice Z-stack. The 3-dimensional volume of TUNEL positive cells was counted using LAS X software.

2.6.4. Assessment of cell cycle

BEAS-2B cells were cultured in serum-free medium for 48 hours to synchronize the cells at the G1/G0 phase and then stimulated with 10% FBS, as previously described [30]. Briefly, the cells were harvested in PBS, fixed with 70% ethanol (vol/vol) at −20 °C and washed twice with cold PBS. The cells were incubated with PI/RNase Staining Buffer (BD Biosciences, Franklin Lakes, NJ) at room temperature for 15 minutes. Data were acquired using the SH 800S sorter/cytometer and analyzed using FlowJo (BD Life Sciences, USA). The assessment of the cell cycle was performed based on the DNA content (PI, fluorescence intensity of staining) of individual cells using forward scatter area *vs.* height plots for the exclusion of cell doublets.

2.6.5. Measurement of mitochondrial fission

Cells were loaded with the potentiometric dye tetramethyl rhodamine methyl ester (TMRM, T668, ThermoFisher Scientific, Burlington, ON, Canada) at 50 nM for 20 minutes in culture medium at 37 °C. Mitochondrial morphology was quantified using two techniques, mitochondrial fragmentation count (MFC) and machine learning. Cells were imaged using a Leica SP8 confocal microscope (Leica Microsystems Inc., Concord, ON, Canada). Images were taken using a 63× 1.4 NA oil immersion objective using the Leica LAS X software (excitation/emission = 561nm/>575 nm). MFC was calculated as the total mitochondrial number divided by the total mitochondrial area in each confocal microscopy image, as described [31]. A higher MFC indicates a more fragmented mitochondrial network. Mitochondrial morphology was also quantified by machine-learning, an unbiased counting algorithm

that trains the computer to classify mitochondria as punctate, intermediate, or filamentous and expresses these groups as the % of total mitochondrial area/cell, as described [31].

2.6.6. Measurement of mitochondrial membrane potential (ΔΨm)

Relative changes in ΔΨm was measured using confocal microscopy in murine airway cells loaded with either tetramethylrhodamine (TMRM), as described [18] or in BEAS-2B cells, using another potentiometric dye, 5,5′,6,6′-tetrachloro-1,1′,3,3′-tetraethylbenzimidazolcarbocyanine iodide (JC-1) and flow cytometry. TMRM is taken up in non-linear proportion to the ΔΨm. The dynamic range of TMRM in airway cells was validated using flow cytometry by treating TMRM-stained BEAS-2B cells with increasing concentrations of carbonyl cyanide-p-trifluoromethoxyphenylhydrazone (FCCP), a potent proton ionophore that dissipates ΔΨm. For microscopy studies, cells were grown in 35 mm glass bottom MatTek dishes and 48 hours following transfection or infection, cells were loaded with TMRM (50 nM for 20 minutes in culture medium at 37 °C; Molecular Probes, Eugene, OR, USA) (n = 15/group), as described [27]. Live cells were placed in a stage top incubator (OkoLabs Bold line series) and imaged on a Leica SP8 confocal microscope using a 63× 1.4 NA objective and white light laser (excitation/emission 560nm/590-610 nm). Emission intensities were measured using LAS X software.

In the JC-1 experiments, BEAS-2B cells were cultured and grown in 35 mm MatTek dishes for 24 hours. One group was transduced with Lenti-M virus and the control group was Mock infected. A third group (also Mock) was treated with the proton ionophore FCCP (1.6 μM for 10 minutes), to establish JC-1's dynamic range of membrane potential detection. All groups were stained with JC-1 at 10 μg/ml for 30 minutes. Dishes were then imaged, recording 20 Fields of view with 4–5 cells per field. JC-1 was excited by a white light laser tuned to 491 nm and red/green fluorescence intensities were measured at 570–625 nm and 520-55 nm, respectively, using HyD detectors and a Leica SP8 microscope. Ratios of Red/Green average intensities were calculated.

2.6.7. Measurement of metabolism (oxygen consumption rates, ATP concentrations and ETC complex I activity)

Mitochondrial metabolism was quantified by measuring oxygen consumption rate and extracellular acidification rate (OCR/ECAR) using Seahorse micropolarimetry, as described [18]. These studies were done both in infected cells (using HCoV-OC43 or MHV-1) or BEAS-2B cells transduced with SARS-CoV-2 proteins. ETC Complex I activity was measured as described [18].

2.6.8. Seahorse micropolarimetry

Mitochondrial metabolism was quantified by measuring oxygen consumption rates and extracellular acidification rates (OCR/ECAR) using an XF24 Extracellular Flux Analyzer (Agilent, Santa Clara, CA). BEAS-2B cells infected with HCoV-OC43 or transduced with SARS-CoV-2 proteins (Nsp7, Nsp9 & M) as well as LA-4 cells infected with MHV-1 were plated at 40,000 per well in a 24-well XF24 cell culture microplate (part #100777–004, Agilent). Cells were allowed to sit in the microplate for either 48 hours (HCoV-OC43), 72 hours (MHV-1), or 96 hours (SARS-CoV-2) before the assay was run. A day prior to the experiment, an extracellular flux assay kit (part #100850–001, Agilent, Santa Clara, CA) was hydrated by loading 1 mL of XF calibrant solution (part #100840–000, Agilent) into each well in the utility plate and incubating at 37 °C overnight in a CO_2 free incubator. The next day, measurements were taken after equilibration in XF assay media (part #102353–100, Agilent) supplemented with 4.5 g/L glucose, with pH adjusted to 7.4 at 37 °C. To measure changes in OCR and ECAR, oligomycin, carbonyl cyanide-4 (trifluoromethoxy) phenylhydrazone (FCCP), and rotenone/antimycin A were added to ports A, B, and C. OCR and ECAR values were normalized after wells were protein quantified using the Pierce™ BCA Protein Assay Kit (catalogue #23227, ThermoFisher Scientific).

2.6.9. Measurement of ATP

ATP levels were measured using the ATP Determination Kit (A22066, ThermoFisher Scientific), a luciferase-luciferin based assay in which luminescence changes in proportion to the presence of ATP. BEAS-2B cells were collected 48 hours post HCoV-OC43 infection and lysed in buffer (20 mM Tris, pH 7.5, 2.5 mM EDTA, 25 mM NaCl, 0.5% Nonidet P-40). After lysis, protein concentration was quantified using the Pierce™ BCA Protein Assay Kit (23227, ThermoFisher Scientific). 0.25 μg of protein from each condition was used per well, and luminescence was measured using a SpectraMax M3 (Molecular Devices, San Jose, CA).

2.6.10. Measurement of complex I activity

Complex I activity was quantified using the Complex I Enzyme Activity Dipstick Assay (ab109720, Abcam, Toronto, ON). BEAS-2B cells were collected either 48 hours post HCoV-OC43 infection or 96 hours post lentiviral transduction with SARS-CoV-2 proteins (Nsp7, Nsp9 & M). After incubation with extraction buffer and centrifugation, protein concentration of supernatants was quantified using the Pierce™ BCA Protein Assay Kit (catalogue #23227, ThermoFisher Scientific). 10 μg of protein from each condition was used per dipstick, and dipsticks were imaged using the ChemiDoc MP Imaging System (Bio-Rad, Mississauga, ON) and analyzed using ImageJ.

2.6.11. Measurement of $[Ca^{2+}]_i$ in PASMC

A rise in $[Ca^{2+}]_i$ in response to acute challenge with hypoxic medium was used as a cellular surrogate for HPV. PASMC from 2 normal subjects, obtained at transplant or autopsy (passage 6–9) were plated on 35 mm, glass-bottom dishes (No. 1.5 uncoated γ-irradiated, MatTek Corporation, Ashland, MA, USA) at a density of 8×10^4 cells per dish and transduced the next day with lentivirus containing GFP (control), M, Nsp7, or Nsp9. After 96 hours, cells were incubated with 10 μM Cal-520 a.m. dye with 0.02% Pluronic F-127 (Invitrogen P6866) for 30 minutes at 37 °C in the dark. Live cell imaging was performed using a Leica TCS SP8 X confocal microscope at 4 frames/minute. PASMC were held in normoxia (PO_2 100 mmHg) and then rapidly changed to hypoxia (50 mmHg for 15 minutes), modulating PO_2 using an OkoLabs stage-top microscope incubator (OkoLab Bold Line, Pozzuoli, Italy). Experiments were conducted at 37 °C (pH 7.35–7.45), as described [18]. To ensure that the viral protein's effects involved inhibition of O_2 sensing (not a non-specific inhibition of calcium flux) cells were challenged with 80 mM KCl.

2.6.12. Murine model of MHV-1 pneumonia (model and hemodynamics)

Five-week-old A/J mice (Jackson Labs, Bar Harbour, Maine; n = 7; male/female = 4/3) were given an intranasal inoculation of either MHV-1 (5000 PFU/17 μl) or an identical volume of saline as control (n = 9/group; male/female = 4/5), as previously described [23,24]. This model causes profound hypoxemia within 1 week of inoculation [23,24]. Mice were monitored daily for disease, measuring weight and transcutaneous O_2 saturation. At day 4–6 post-infection, mice were anesthetized with a single IP injection of ketamine/xylazine (150 mg/kg and 10 mg/kg, respectively). O_2 saturation was measured while mice breathed room air, following which they were intubated and mechanically ventilated, which increased their O_2 saturation. Transcutaneous O_2 saturation was monitored during the procedure using a MouseSTAT® Jr. rodent pulse oximeter attached to the rear paw (Kent Scientific Corporation, Torrington, CT, USA). Right heart catheterization (RHC) was performed using a 1.2F Scisense pressure-volume catheter (Transonic Systems Inc., Ithaca, NY, USA) via a closed chest approach, as described [32]. Mice were ventilated with normoxic gas (room air, 20.6% O_2) followed by hypoxic gas for 10 minutes (10% O_2 balanced with N_2). After the first hypoxic challenge, mice were ventilated with normoxia and after ~5 minutes, the Ca_L channel agonist BAY K8644 (5 mg/kg, IP) [33], was administered. After 5 minutes the mice were subject to a second hypoxic challenge for 10 minutes and the magnitude of HPV and systemic

oxygen saturation (SpO_2) in the presence of BAY K8644 was determined.

2.6.13. Micro-computed tomography (micro-CT)

Lungs were fixed with 4% formaldehyde (PFA) and perfused with 25% barium sulfate via the trachea and imaged by microCT. The micro-CT images were acquired using a VECTor4CT pre-clinical scanner (MILabs B.V., Utrecht, Netherlands) equipped with a cone beam X-ray CT system. The measurements used an acceleration voltage of 50 kVp and X-ray tube current of 430 μA in the ultra-focus mode, allowing acquisition of 3,600 projections with exposure time 40 ms, resulting in a 25 μm resolution. The tomographic CT images were reconstructed using MILabs reconstruction software. For quantification and segmentation, reconstructed slice data were manually processed using PMOD 3.9 software (PMOD Technologies Ltd., Zurich, Switzerland).

2.6.14. Histology

Murine lungs were harvested, then perfused and immersed in 4% paraformaldehyde for 24 hours. Tissues were then processed with a Leica HISTOCORE Pearl tissue processor and sections 4 μm in thickness were made using a Leica HISTOCORE Multicut microtome. Sections were baked for 1 hour on a glass slide. Hematoxylin and eosin staining was performed as previously described [34].

2.6.15. Transmission electron microscopy (TEM)

BEAS-2B cells infected with HCoV-OC43 for 72 hours were fixed in 2.5% glutaraldehyde followed by osmium tetroxide. After fixation, the cells were processed through ascending grades of ethanol, propanol and EMbed 812 epoxy resin. Ultrathin sections were cut and stained with Reynold's lead citrate and 5% uranyl acetate. The sections were imaged using an FEI Tecnai TEM (Hillsboro, Oregon). Mitochondrial diameter was measured in control and infected cells (n = 40 each) using Gatan DigitalMicrograph 3.4 software and analyzed using Welch's two sample T-test.

3. Results

3.1. Transcriptomic changes induced by replicating SARS-CoV-2 in Calu-3 AEC

We reanalyzed RNA-Seq data from our published work to show the effects of confirmed infection on differential gene expression at time-points from 0 to 12 hours post infection (Supplemental File 1). We also examined the data set for enriched gene ontology (GO) pathways (Supplemental File 2). At 2 hours post infection, there is a significant enrichment of 1,255 pathways (corrected $p<0.01$). When organized according to the count of genes within each function, the second most enriched GO pathway was *mitochondrial matrix* (*GO*:0005759; Fig. 1A).

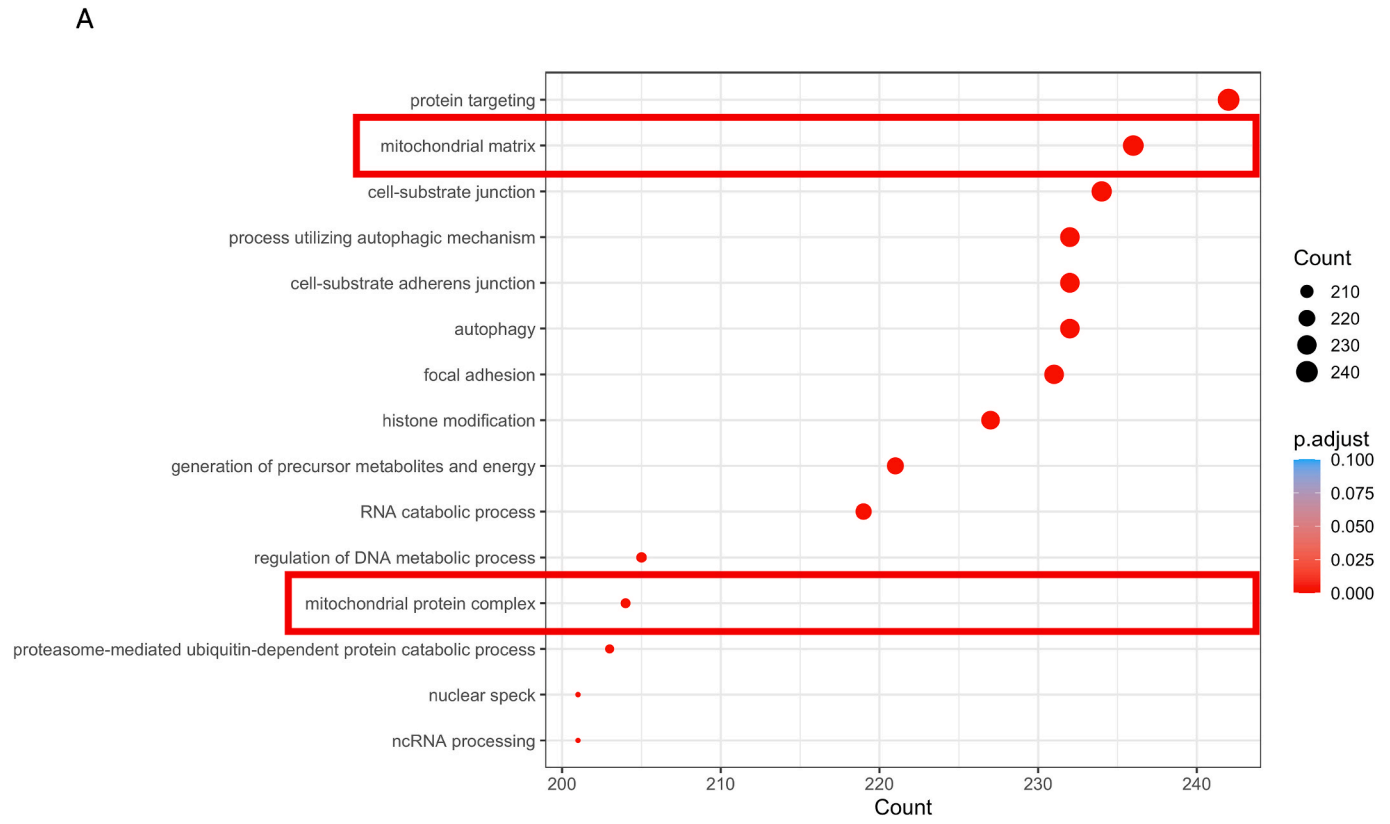

Fig. 1. Infection of human AEC with SARS-CoV-2 regulates mitochondrial GO pathways at 2 hours. Transcriptomics was performed in control vs. infected Calu-3 human airway epithelial cells and Gene Ontology (GO) analysis was performed at each timepoint. These results were filtered to reveal those functions associated with mitochondria (see Data Supplemental File 2).

A) A subset of GOterms organized by gene count reveal enriched GO functions enriched at 2 hours infection. All GOterms are significant (Benjamini & Hochberg corrected $p < 0.05$), and circle size/x-axis reflects gene number in each GO cluster. The second most enriched GOterm (from a list of 1,255 terms), when organized by gene count, is mitochondrial matrix, which represents the expression of over 230 genes.

B) A subset of GOterms organized by gene count reveal significant GOterms associated with mitochondria that are enriched at 2 hours post-infection. GOterms regulating mitochondrial membrane permeability, electron transport and metabolism, as well as other apoptotic pathways are enriched. The most regulated cellular component within the mitochondria is the matrix.

C) Pathway analysis shows the key genes regulated at 2 hours within the GO term, mitochondrial matrix, selected because this term had the largest number of significantly regulated genes.

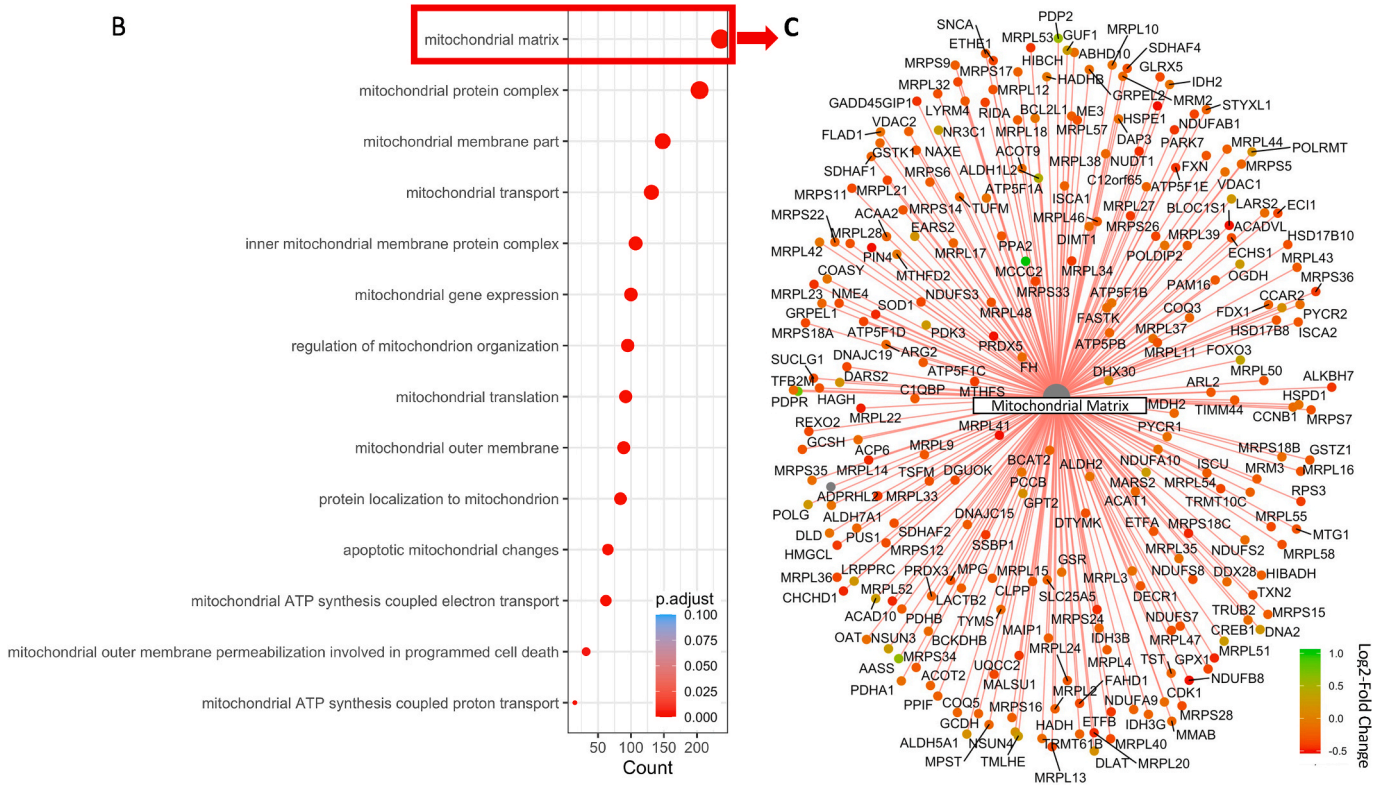

Fig. 1. (*continued*).

This GOterm reflected the expression of over 230 genes and was second only to *protein targeting* in the number of regulated genes. When we filtered this list to look for other enriched mitochondrial functions using the string "mito", we saw modulation of numerous mitochondrial GO pathways (Fig. 1B). These pathways were relevant to *apoptosis (GO:0008637)* (Table 1)*, mitochondrial outer membrane permeabilization (GO:1901030), mitochondrial ATP synthesis coupled electron transport (GO:0042775)* and *proton transport (GO:0042776)*. The regulated genes associated with the *mitochondrial matrix* are shown in Fig. 1C.

Multiple genes related to the function of ETC Complex I were significantly down-regulated in SARS-CoV-2 infected cells, including *NDUFAB1, NDUFS7* and *NDUFS8* (Table 2). Genes relevant to bioenergetics and ATP synthesis were also significantly downregulated within 2 hours of SARS-CoV-2 infection, including: *PDHB*, *ATP5F1b*, and *ATP5B* (Table 2). There were also some strongly upregulated genes involved in bioenergetic pathways at 2 hours post-infection, including *MCCC2*, *PDP2*, and *PDPR* (Table 2).

Filtering the list of enriched GO terms containing the string "apop", we identified 25 overlapping terms that were enriched at 2 h (Fig. 2A, Table 1), including 5 terms that explicitly refer to mitochondrial functions associated with apoptosis, notably *apoptotic mitochondrial changes (GO:0008637)*. Fig. 2B shows a heat map of the most upregulated apoptotic genes 2 hours post-infection, a list which includes *BCL2L11 (*BIM), *CCAR2*, *PPP1R13B, YWHAG*, *TP53BP2, WDR35,* and *ATF2* (Table 2). *DNM1L,* the gene encoding the mitochondrial fission mediator dynamin-related protein 1 (Drp1), was also upregulated. Consistent with this, SARS-CoV-2 caused significant mitochondrial fission in human AEC (Fig. 3A–C).

3.2. Protein expression induced by replicating SARS-CoV-2 in Calu-3 AEC

We used immunofluorescence (Fig. 3D–E) and immunoblots (Fig. 3F–I) to confirm upregulation of several key mediators identified by transcriptomics in cells in which SARS-CoV-2 infection was confirmed by measuring the expression of its nucleocapsid protein (Fig. 3F). Immunofluorescence confirmed that infection upregulated the expression of total Drp1 and activated Drp1 protein (i.e. Drp1 phosphorylated at serine 616, p-Drp1$_{S616}$) in mitochondria (Fig. 3D–E). Immunoblots verified the increased expression of Drp1 and p-Drp1$_{S616}$, demonstrating a large increase in the ratio of activated to total Drp1 (Fig. 3G). Immunoblots also confirmed that SARS-CoV-2 infection increased the expression of a key mediator in the mitochondrial apoptosis pathway, AIF (Fig. 3H). Moreover, SARS-CoV-2 activated the mitochondrial apoptosis pathway, demonstrated by increased expression of the activated(cleaved) caspase 7, without altering total caspase 7 expression (Fig. 3I).

3.3. Replicating HCoV-OC43 in BEAS-2B AEC and HPAEC

HCoV-OC43 infection, confirmed by the expression of its nucelocapsid protein, induced a mitochondriopathy characterized by: increased expression of apoptosis mediators BiD, AIF, Smac/DIABLO, and caspase 1 in AEC (Fig. 4A). HCoV-OC43 infection also impaired metabolism [reduced basal and maximal O_2 consumption rate (OCR) and reduced ATP-linked OCR (Fig. 4Bi-iv)]. Consistent with the transcriptomic effects on ETC Complex I gene expression seen with SARS-CoV-2, HCoV-OC43 reduced ATP levels in infected BEAS-2B cells (Fig. 4Bv) and inhibited ETC Complex I activity (Fig. 4Bvi). As with SARS-CoV-2 infection, HCoV-OC43 infection also increased the expression of p-Drp1$_{S616}$ (Fig. 4Aii) and increased mitochondrial fission in both BEAS-2B cells (Supplemental Fig. 4B) and human pulmonary artery endothelial cells (Fig. 4C). Confocal stimulation emission depletion (STED) microscopy shows that the nucleocapsid protein of HCoV-OC43 is adjacent to AIF on the mitochondrial membrane, demonstrating the mitochondrial localization of viral proteins (Fig. 4Aviii). Using STED microscopy, we show that HCoV-OC43 infection tends to increase AIF expression and significantly increases fission (Supplemental Figs. 4A–B). TEM shows the mitochondria in HCoV-OC43-infected BEAS-2B cells are significantly swollen and identifies viral particles within AEC vesicles

Table 1
Regulated genes in the SARS-COV-2 apoptotic march: List of significantly enriched GOterms related to apoptosis derived from differentially regulated genes at 1, 2 and 12 hours post infection with SARS-CoV-2. Briefly, differentially regulated genes identified at each time point were parsed through gene ontology GO analysis software and the output was filtered using the string 'apop' in order to identify those functions that related by name to apoptosis. Definitions: **GO-ID:** Gene Ontology Identification, **Description:** functional annotation of GO-ID, **p-adjust:** Benjamini & Hochberg corrected p-value, **q.value:** False discovery rate, **Gene Count:** Number of differentially regulated genes contributing towards function at each experimental timepoint.

GO-ID	Description	p-adjust	q. value	Gene Count
1 h post-infection				
GO:1900118	Negative regulation of execution phase of apoptosis	8.28E-03	7.50E-03	7
2 h post-infection				
GO:0097193	Intrinsic apoptotic signaling pathway	6.55E-09	5.02E-09	140
GO:2001235	Positive regulation of apoptotic signaling pathway	1.39E-08	1.07E-08	90
GO:2001233	Regulation of apoptotic signaling pathway	1.53E-07	1.17E-07	173
GO:2001242	Regulation of intrinsic apoptotic signaling pathway	1.96E-06	1.50E-06	80
GO:0008637	Apoptotic mitochondrial changes	4.67E-06	3.57E-06	65
GO:0043281	Regulation of cysteine-type endopeptidase activity involved in apoptotic process	8.87E-06	6.80E-06	101
GO:0043280	Positive regulation of cysteine-type endopeptidase activity involved in apoptotic process	8.08E-05	6.19E-05	67
GO:0070059	Intrinsic apoptotic signaling pathway in response to endoplasmic reticulum stress	9.01E-05	6.90E-05	37
GO:2001244	Positive regulation of intrinsic apoptotic signaling pathway	1.12E-04	8.56E-05	32
GO:0008630	Intrinsic apoptotic signaling pathway in response to DNA damage	3.89E-04	2.98E-04	54
GO:0097191	Extrinsic apoptotic signaling pathway	4.55E-04	3.49E-04	97
GO:0072332	Intrinsic apoptotic signaling pathway by p53 class mediator	6.72E-04	5.15E-04	41
GO:0006919	Activation of cysteine-type endopeptidase activity involved in apoptotic process	9.19E-04	7.04E-04	46
GO:1901030	Positive regulation of mitochondrial outer membrane permeabilization involved in apoptotic signaling pathway	1.16E-03	8.85E-04	20
GO:0051402	Neuron apoptotic process	1.40E-03	1.07E-03	92
GO:2001238	Positive regulation of extrinsic apoptotic signaling pathway	1.43E-03	1.10E-03	27
GO:0043525	Positive regulation of neuron apoptotic process	1.78E-03	1.36E-03	26
GO:2001243	Negative regulation of intrinsic apoptotic signaling pathway	2.33E-03	1.79E-03	46
GO:1902229	Regulation of intrinsic apoptotic signaling pathway in response to DNA damage	2.80E-03	2.15E-03	22
GO:0030262	Apoptotic nuclear changes	2.84E-03	2.17E-03	20
GO:0042771	Intrinsic apoptotic signaling pathway in response to DNA damage by p53 class mediator	3.53E-03	2.70E-03	26
GO:1900739	Regulation of protein insertion into mitochondrial membrane involved in apoptotic signaling pathway	4.96E-03	3.80E-03	15
GO:1900740	Positive regulation of protein insertion into mitochondrial membrane involved in apoptotic signaling pathway	4.96E-03	3.80E-03	15
GO:0001844	Protein insertion into mitochondrial membrane involved in apoptotic signaling pathway	5.34E-03	4.09E-03	17
GO:0006921	Cellular component disassembly involved in execution phase of apoptosis	6.21E-03	4.76E-03	20
12 h post-infection				
GO:0042771	Intrinsic apoptotic signaling pathway in response to DNA damage by p53 class mediator	1.16E-03	1.02E-03	6
GO:0072332	Intrinsic apoptotic signaling pathway by p53 class mediator	2.20E-03	1.94E-03	7
GO:0097193	Intrinsic apoptotic signaling pathway	2.23E-03	1.96E-03	13

(Fig. 4Bvii-ix).

3.4. SARS-CoV-2 transduction of human AEC

Transduction efficacy: We confirmed the successful expression of SARS-CoV-2 proteins in A549 cells transduced with each lentiviral vector (Supplemental Fig. 1) before applying these vectors to study AECs. Transduction rates, measured by GFP fluorescence, were ~29% in A549 cells and maximal transfection was achieved by 96 hours (Supplemental Fig. 2). Similar transduction rates were observed in BEAS-2B.

Depolarization of ΔΨm: Transduction with the SARS-CoV-2 M protein depolarized mitochondrial membrane potential in BEAS-2B cells, as measured using the potentiometric dye JC-1 (Supplemental Fig. 6C and D).

Activation of AIF and induction of apoptosis: Transduction with Nsp7, Nsp9, or M proteins upregulated AIF in BEAS-2B cells (Fig. 5A–B), and triggered apoptosis in BEAS-2B cells (Fig. 5C). While all three SARS-CoV-2 proteins increased AIF expression and caused apoptosis, only the M protein reduced the expression of the cyclin kinase (CDK4), which is a positive regulator of cell cycle progression (Fig. 5A). Consistent with this, only M protein transduction triggered G1-G0 cell cycle arrest (Fig. 5D). Likewise HCoV-OC43 infection reduced CDK4 expression in AEC (Fig. 4Aiii). Consistent with the observation that SARS-CoV-2 infection regulated GO pathways regulating *mitochondrial outer membrane permeability involved in programmed cell death* (Fig. 1B), transduction with the M protein increased opening of the mPTP, an initiating step of apoptosis (Fig. 5E).

Mitochondrial fission: Transduction of each of the tested SARS-CoV-2 proteins increased Drp1 expression and activation (Fig. 5A), consistent with the observed increase in activated Drp1 expression that follows SARS-CoV-2 infection (Fig. 3D–G). Nsp7 and Nsp9 also increased mitochondrial fission in BEAS-2B cells (Supplemental Fig. 3), consistent with the increase in mitochondrial fission that resulted from SARS-CoV-2 infection of AEC (Fig. 3A–C) and HCoV-OC43 infection of HPAEC (Fig. 4C and Supplemental Figs. 4A–B).

Inhibition of oxidative metabolism: Transduction with Nsp7 uniquely reduced basal and maximal OCR (Supplemental Figure 5A, D-E), ATP-linked OCR, and proton leak in BEAS-2B cells (Supplemental Figs. 5F–G). Similar inhibition of OCR occurred with HCoV-OC43 infection of BEAS-2B cells (Fig. 4Bi-iv). Transduction with Nsp7 and HCoV-OC43 infection also inhibited the activity of ETC Complex I (Supplemental Figure 5C and Fig. 4Bvi), and HCoV-OC43 infection also reduced ATP concentrations in BEAS-2B cells (Fig. 4Bv). It is noteworthy that these negative effects on metabolism do not reflect nonspecific mitochondrial toxicity from lentiviral transduction of heterologous proteins. We demonstrated this by showing that transduced GFP did not cause protein aggregation nor did it damage or interact with mitochondria, whereas the M protein, which did trigger apoptosis, localized on the mitochondrial outer membrane on STED microscopy (Supplemental Fig. 6E).

Table 2
The most regulated genes following SARS-CoV-2 infection by functional category: *Differentially regulated genes at 2 hours post-infection with SARS-CoV-2.* **Definitions: Ensemble gene id:** Unique Gene ID provided by Ensembl, **Gene Symbol:** Unique gene symbol, **Function:** Gene function described within the context apoptosis, ETC Complex I, and Bioenergetics and ATP synthesis, Log2-Fold Change: Differentially regulated gene log2 fold change, **p.adjust:** Benjamini & Hochberg corrected p-value.

Ensemble gene id	Gene symbol	Function	log2 Fold Change	p. adjust
Apoptosis Genes				
ENSG00000153094	BCL2L11 (BIM)	Interacts with dynein light chain 1 and induce apoptosis by inactivating anti-apoptotic BCL2 proteins and/or by activating BAX-BAK	0.28	3.8E-03
ENSG00000158941	CCAR2	In response to TNFα it is cleaved by caspases and the resulting truncated proteins promote mitochondrial clustering and apoptotic cell death	0.14	1.0E-03
ENSG00000088808	PPP1R13B	Encodes an ASPP (apoptosis-stimulating protein of p53) which promotes DNA binding and transactivation of p53-family proteins on the promoters of proapoptotic genes	0.24	2.7E-03
ENSG00000082701	GSK3B	Promotes apoptosis via the intrinsic pathway	0.11	2.5E-02
ENSG00000170027	YWHAG	Member of the 14.3.3 protein group	0.14	6.5E-03
ENSG00000143514	TP53BP2	Enhancing TP53 DNA binding and the transactivation function of TP53 on the promoters of proapoptotic genes	0.21	4.7E-04
ENSG00000118965	WDR35	Bind to phosphoserine-containing proteins involved in metabolism, apoptosis, and cell cycle regulation	0.32	9.7E-04
ENSG00000115966	ATF2	Interacts with BIM at the mitochondrial outer membrane resulting in reduced mitochondrial membrane potential and leakage of proapoptotic mediators	0.19	3.5E-03
ETC Complex I Genes				
ENSG00000004779	NDUFAB1	A Complex I subunit which enhances the capacity and efficiency of mitochondrial energy metabolism by coordinating the assembly of ETC Complexes, and by regulating iron-sulfur biosynthesis and Complex I stability	−0.39	3.0E-16
ENSG00000115286	NDUFS7	Involved in ETC Complex I electron transfer and assembly	−0.33	8.3E-05
ENSG00000110717	NDUFS8	Involved in ETC Complex I electron transfer and assembly	−0.34	6.4E-07
Bioenergetics and ATP synthesis Genes				
ENSG00000168291	PDHB	Component of the enzyme, pyruvate dehydrogenase (PDH) which catalyzes the conversion of pyruvate to acetyl-CoA. It also regulates glucose oxidation during pathologic conditions, such as cardiac hypertrophy	−0.256	1.6E-08
ENSG00000110955	ATP5F1b	Which encode subunits of mitochondrial ATP synthase	−0.10	1.2E-03
ENSG00000116459	ATP5B	Which encode subunits of mitochondrial ATP synthase	−0.22	4.0E-11
ENSG00000131844	MCCC2	Encodes the small subunit of 3-methyl-crotonyl-CoA carboxylase.	1.06	4.8E-04
ENSG00000172840	PDP2	A mitochondrial protein that functions as a phosphatase and is involved in the enzymatic resetting of the pyruvate dehydrogenase complex.	0.59	1.0E-05
ENSG00000090857	PDPR	Catalyzes the oxidative decarboxylation of pyruvate and links glycolysis to the tricarboxylic acid cycle and fatty acid synthesis	0.788	4.8E-23

3.5. SARS-CoV-2 transduction of human PASMC

Inhibition of hypoxic rise in $[Ca^{2+}]_i$ in human PASMC: Normal human PASMC display a robust rise in $[Ca^{2+}]_i$ in response to acute hypoxia. Transduction with the SARS-CoV-2 M or Nsp9 proteins (~100% transduction at 96 h) attenuated the hypoxic rise in $[Ca^{2+}]_i$, without altering the KCl response, indicating a selective inhibition of HPV (Fig. 6).

Replicating MHV-1 in murine cells and in A/J mice in vivo: MHV-1 infection resulted in a reduction of TMRM fluorescence intensity in murine LA-4 lung adenoma cells (Fig. 7A). This is interpreted as a relative reduction in ΔΨm (Supplemental Fig. 6A), as semi quantified by demonstration of a dose dependent reduction in the TMRM signal by the proton ionophore, FCCP. These findings of coronavirus-induced mitochondrial depolarization are consistent with the depolarization of ΔΨm observed using a different potentiometric dye, JC-1, following M protein transduction of BEAS-2B cells (Supplemental Figs. 6C–D). Like SARS-CoV-2 infection (Fig. 3H), SARS-CoV-2 protein transduction (Fig. 5A–B) and HCoV-OC43 infection (Fig. 4Avii), MHV-1 infection increased the expression of AIF in mitochondria and caused AIF activation, evident as translocation of AIF from the mitochondria to the nucleus (Fig. 7B). As with the human betacoronaviruses, MHV-1 infection impaired metabolism, reducing basal and maximal respiration, proton leak, spare respiratory capacity and ATP-linked OCR (Supplemental Fig. 7). Similar metabolic impairment was induced by HCoV-OC43 infection (Fig. 4Bi-iv) and SARS-CoV-2 protein transduction (Supplemental Fig. 5).

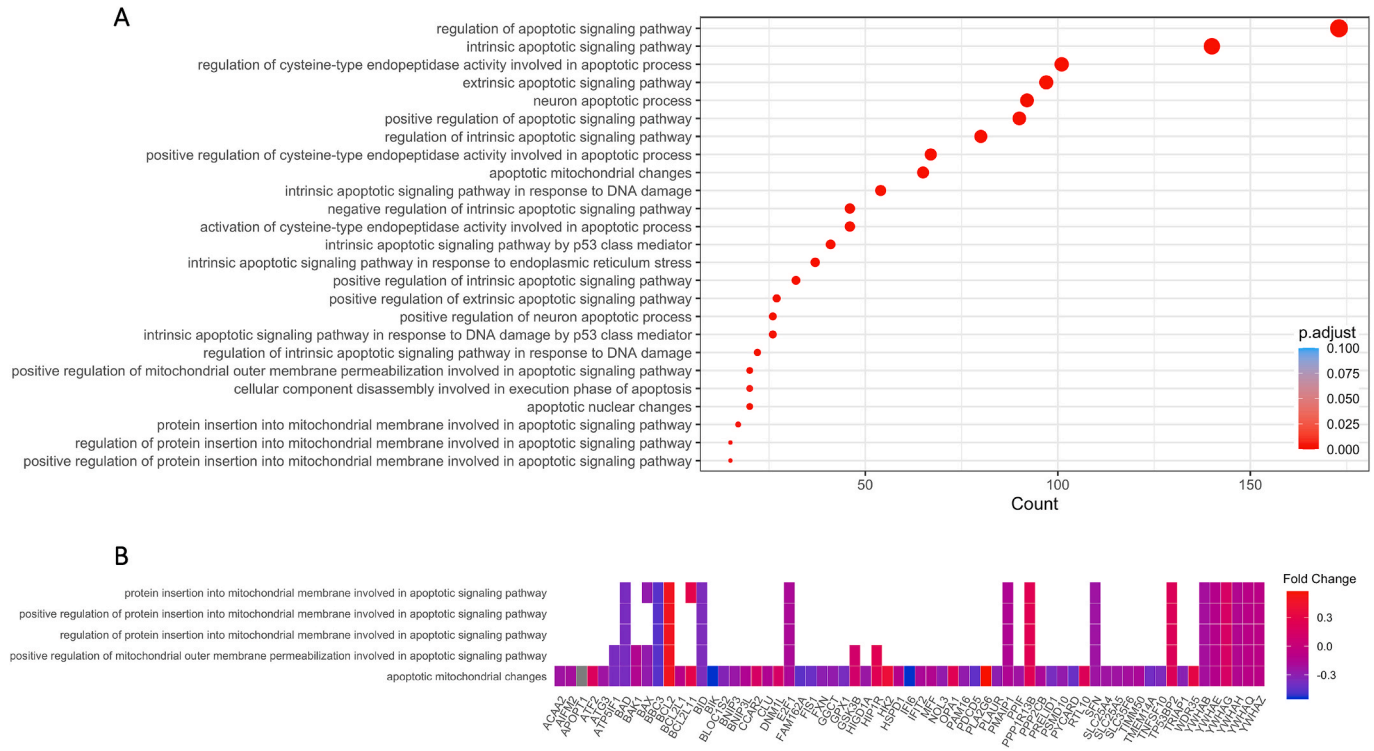

Fig. 2. SARS-CoV-2 infection regulates pro-apoptotic mitochondrial GO pathways at 2 hours. Transcriptomics was performed in control vs. infected Calu-3 human airway epithelial cells and Gene Ontology (GO) analysis was performed at each timepoint. These results were filtered to reveal those functions associated with apoptosis (Data Supplemental File 2) .

A) At 2 hours, there is marked enrichment of GO pathways favoring the induction of mitochondrial-mediated apoptosis. All effects are significant (Benjamini & Hochberg corrected $p < 0.05$) and circle size/x-axis reflect the number of genes within each GO cluster.

B) Heat map showing the most regulated genes relating to apoptosis in infected cells. Even at this early time point there is regulation of pathways favoring mitochondrial-mediated apoptosis.

Within 6 days of nasal inoculation with MHV-1, both male and female mice had marked infiltrates on micro-CT scans, systemic arterial O_2 desaturation, and almost complete inhibition of HPV (Fig. 7Ci-iv). We confirmed MHV-1 infection by immunofluorescence staining with an Nsp9 antibody (Fig. 7Cv). The calcium channel agonist BAY K8644 [35] increased HPV (Δ RVSP 30.6 ± 5.8 mmHg in control mice vs Δ RVSP 26.3 ± 5.3 mmHg in mice with MHV-1 pneumonia) and significantly improved SpO_2 (+3.0 ± 1.0% in control mice vs +2.5 ± 1.2% in MHV-1 mice, Fig. 7Ciii). Histology revealed a lymphocytic infiltrate in the MHV-1 infected lungs (Fig. 7Civ). MHV-1 infection resulted in widespread apoptosis of AECs, as detected by TUNEL staining and all TUNEL positive nuclei were also infected, evident from expression of the MHV-1 Nsp9 protein (Fig. 7Cv).

4. Discussion

Here we report that replicating SARS-CoV-2 and SARS-CoV-2 proteins cause a mitochondriopathy affecting AEC, in the airway, and PASMC and PAEC, in the pulmonary vasculature. Two pathologic consequences of this mitochondriopathy, induction of AEC apoptosis and inhibition of HPV, likely contribute to alveolar damage and hypoxemia in COVID-19 pneumonia (Fig. 8). Additional hallmarks of this SARS-CoV-2 mitochondriopathy (observed in response to multiple coronaviruses) include increased Drp1-mediated mitochondrial fission and impaired mitochondrial bioenergetics (associated with impaired ETC Complex I activity and reduced ATP levels). The features of this SARS-CoV-2 mitochondriopathy are replicated by infections with other beta-coronaviruses, including the human pathogen, HCoV-OC43, and the murine pathogen, MHV-1.

We show that coronavirus-induced mitochondriopathy is: 1) highly conserved, occurring with infection by three different coronaviruses; 2) ubiquitous, occurring in all lung cell types tested (AEC, PASMC and HPAEC); 3) rapid in onset (evident within 2 hours at the level of transcriptomic regulation of mitochondrial GO pathways involved in apoptosis, mitochondrial ETC function, mitochondrial membrane permeability, ATP synthesis, oxidative metabolism, and mitochondrial fission), and 4) recapitulated by heterologous expression of SARS-CoV-2 proteins [17], indicating that the mitochondrial damage is not solely the result of inflammation or a non-specific response to infection.

4.1. Induction of apoptosis

We observed widespread regulation of mitochondrial-mediated apoptosis GO pathways in AEC within 2 hours of SARS-CoV-2 infection (Figs. 1–2, Table 1), including the *positive regulation of mitochondrial outer membrane permeabilization involved in apoptotic signaling pathway (GO:1901030),* a pathway which includes many genes involved in regulating the early steps in apoptosis. This apoptotic march grows over time so that within 12 hours of infection there was regulation of over 140 genes in the *intrinsic apoptotic signaling pathway (GO:0097193,* Table 1). Among the most upregulated, pro-apoptotic genes 2 hours post-SARS-CoV-2 infection were *BCL2L11* [36], *CCAR2* [37], *PPP1R13B* [38], *GSK3b* [39], *YWHAG* [40,41], *TP53BP2* [42], *WDR35* [43] and *ATF2* [44] (Table 2). The biologic relevance of these pro-apoptotic transcriptomic findings is supported by the observation that all tested coronaviruses induce apoptosis in AEC both *in vitro* (Fig. 5C) and *in vivo* (Fig. 7Cv). For example, we show that SARS-CoV-2 infection activates apoptosis pathways, increasing the expression of AIF and activating caspase 7 (Fig. 3H–I). Moreover, heterologous expression of SARS-CoV-2 proteins significantly increases the prevalence of Annexin V positive

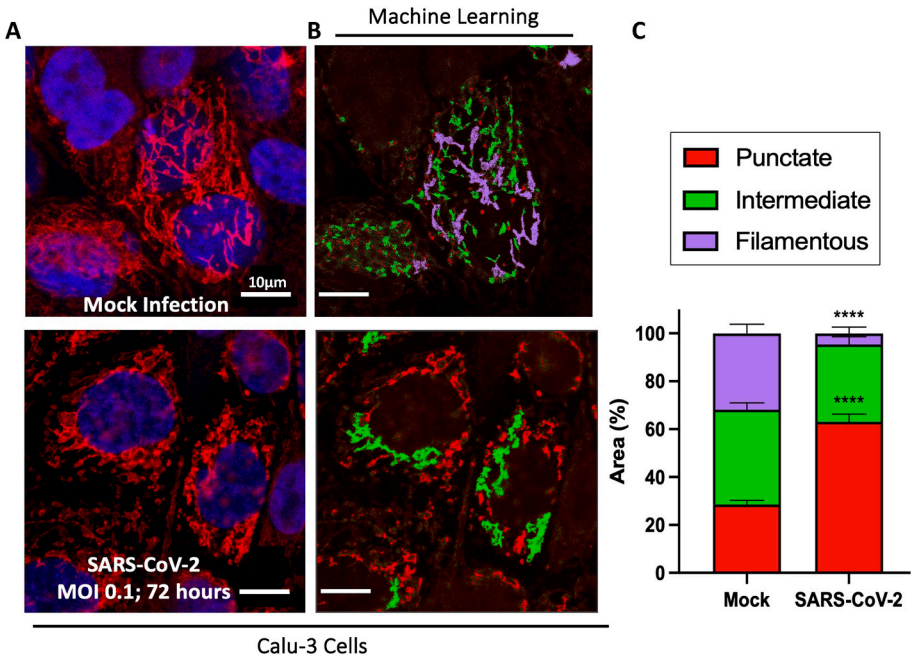

Fig. 3. SARS-CoV-2 infection of Calu-3 human AEC causes mitochondrial fission.

A) Calu-3 cells were infected with SARS-CoV-2 for 72 hours and then loaded with TMRM, revealing mitochondrial structure (red), and DAPI, identifying the nucleus (blue). Infection causes mitochondrial fission, evident as mitochondrial fragmentation. Scale bar = 10 μm.

B–C) Mitochondrial fission was quantified by machine learning, which uses an algorithm to automatically categorize and colour code mitochondria as punctate, intermediate, or filamentous, as described [31]. Quantitative analysis shows that SARS-CoV-2 significantly increases the percentage area of punctate mitochondria and reduces the number of filamentous mitochondria. (****$P < 0.0001$; n = 21 cells/group).

D-E) Confocal imaging shows increased expression of activated and total Drp1 48 hours post SARS-CoV-2 infection. Tomm 20 is used to image the mitochondria (red) with p-Drp1$_{S616}$ and Drp1 imaged in green. Scale bar = 2–15 μm. Representative images (i), 400% zoom (ii) and mean data (iii) are shown. (***$P < 0.001$ n = 5/group). The mean data in panel iii derive from analysis of the low power images (Di and Ei). Note the increase in p-Drp1$_{S616}$ primarily occurs in the mitochondria, seen as increased yellow (from red/green colocalization in low power images, Di) and seen directly on high power STED images (Dii), with most green p-Drp1$_{S616}$ localizing to the mitochondrial outer membrane,

F–I) Immunoblot confirms that SARS-CoV-2 infection increases the expression of activated Drp1, increases the expression of the apoptosis mediator AIF and activates caspase 7.

(F) Marked increase in SASR-CoV-2 N protein expression only in infected cells confirms infection. The Calu-3 cells were harvested for immunoblot analyses after 48 hours of infection with SARs-C0V-2. Representative image of the immunoblots and the densitometry of the expressions of (G) p-Drp1$_{ser616}$, (H) AIF and (I) cleaved caspase 7. (*$P < 0.05$; **$P < 0.01$; n = 3–5 technical replicates/group).

AEC, reflecting increased apoptosis (Fig. 5C). In terms of mechanism of apoptosis induction, we show that SARS-CoV-2 M protein opens the mPTP (Fig. 5E) and depolarizes ΔΨm (Supplemental Figs. 6C–D), which are the initial steps in apoptosis.

HCoV-OC43 infection also increased the expression of apoptosis mediators (e.g., Bid, Smac/DIABLO, AIF, and caspase 1; Fig. 4Aiv-vii), consistent with apoptosis being a conserved toxicity of human coronaviruses. Although MHV-1 differs from SARS-CoV-2 in its species specificity and cellular receptor, it reproduces many of the mitochondrial toxicities seen with human betacoronaviruses. For example, MHV-1 depolarizes ΔΨm (Fig. 7A, Supplemental Figs. 6A–B), increases the expression and activity of AIF (Fig. 7B) and causes apoptosis of AEC in the MHV-1 pneumonia model (Fig. 7Cv).

Our results are consistent with a 2022 report by Ramachandran et al. that human peripheral blood mononuclear cells infected with SARS-CoV-2 had changes in mitochondrial-relevant gene expression, favoring apoptosis and mitochondrial fission [13]. Ramachandran et al. also found that transduction with SARS-CoV-2 proteins (M, NSP6, ORF3A, ORF9C, and ORF10) results in protein interactions with components of the mPTP complex, including cyclophilin D, SPG-7, ANT, ATP synthase, and CCDC58. Moreover, they reported that the mPTP blocker cyclosporin A prevented a SARS-CoV-2-induced reduction of mitochondrial calcium retention capacity and preserved bioenergetics in cardiomyocytes [13]. However, unlike our study, they did not evaluate lung cells or tissues and included no *in vivo* studies.

The widespread AEC apoptosis we observed in the MHV-1 pneumonia model (Fig. 7Cv) is consistent with AEC apoptosis seen in the SARS-CoV-2 pneumonia model in Syrian Golden hamsters [45]. Moreover, Thompson et al. recently showed that a nonclonal T cell population in COVID-19 patients has dysmorphic mitochondria and increased cytoplasmic cytochrome *c* levels, consistent with induction of apoptosis [46]. Since apoptosis is a surrogate for cell death and lung injury, our findings are also consistent with the observation that elevated levels of circulating mitochondrial DNA in COVID-19 pneumonia patients predict poor outcomes [47]. In 2022, Yang et al. showed that transduction of AEC with SARS-CoV-2 M protein induced mitochondrial apoptosis [48] by inhibiting the ubiquitination of B-cell lymphoma 2 (BCL-2)-related ovarian killer (BOK), thereby stabilizing BOK, and promoting mitochondrial translocation. Our findings support their conclusions and we extend their work by demonstrating the proapoptotic effects of coronavirus infections using replicating SARS-CoV-2 and identifying a conserved role for AIF in this apoptotic pathway.

SARS-CoV, the coronavirus which caused the SARS epidemic, also triggers apoptosis in human cells [8,9]. Both SARS-CoV infection and heterologous expression of SARS-CoV's E protein cause apoptosis in T cells [49]. We observed similar effects on AEC mitochondria in response to SARS-CoV-2 infection versus transduction with SARS-CoV-2 Nsp and M proteins. Both infection and transduction activate pathways that lead

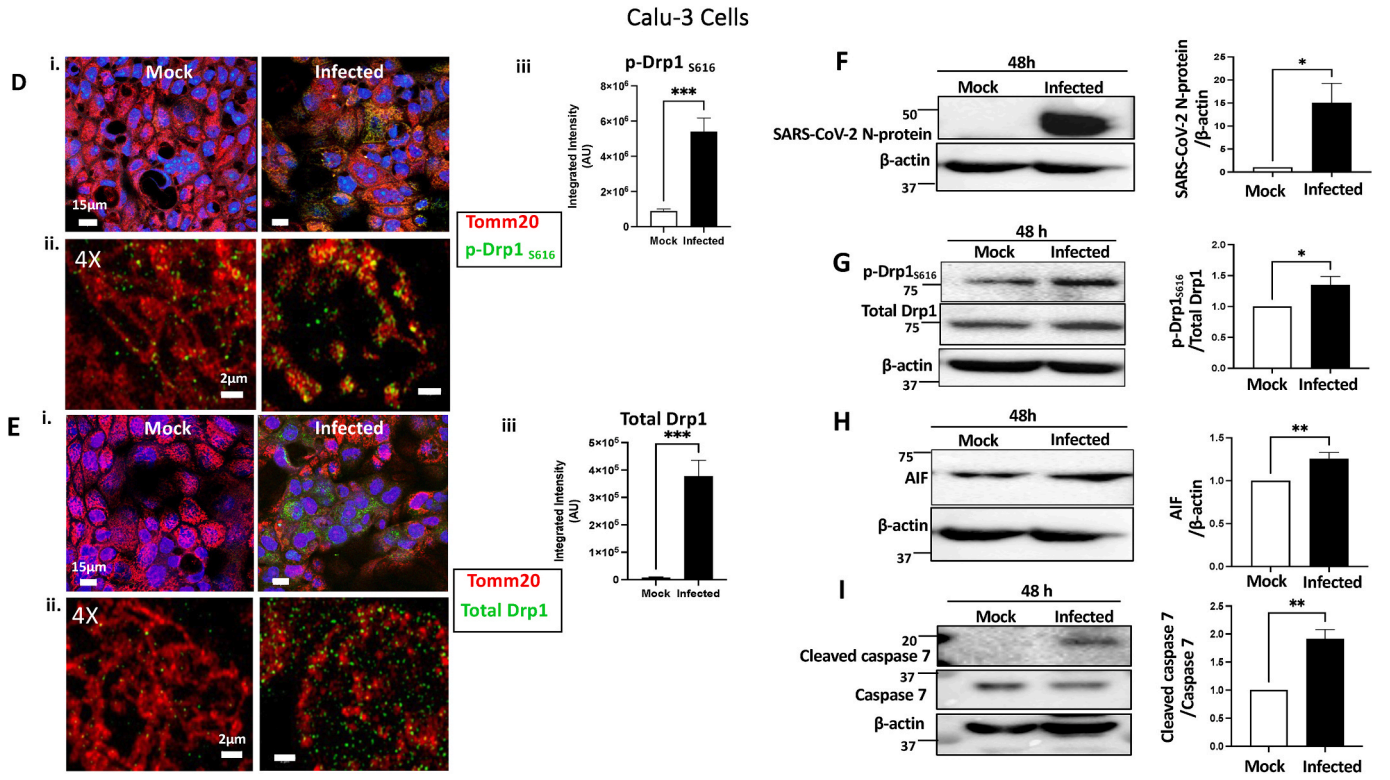

Fig. 3. (*continued*).

to apoptosis and mitochondrial fission in AEC. Moreover, SARS-CoV upregulates proapoptotic mediators like Bid [16], AIF, cytochrome *c* [50] and caspase 8 [51], consistent with the caspase 7 activation and upregulation of AIF we observed with SARS-CoV-2 infection (Fig. 3H–I) and the upregulation of Smac/DIABLO, caspase 1, Bid, and AIF we observed with HCoV-OC43 (Fig. 4Aiv-vii) infections. These parallels between SARS-CoV and SARS-CoV-2 and HCoV-OC43 suggest that mitochondrial-mediated apoptosis is a common feature of pathogenic human coronaviruses.

4.2. Bioenergetics and ETC complex I

SARS-CoV-2 infection also regulated many genes related to ETC Complex I and bioenergetics (Figs. 1–2, Table 2). The net effect of these changes in gene expression would be predicted to include impaired bioenergetics and ETC Complex I function, which we indeed observed (Fig. 4Bi-vi and Supplemental Figs. 5A–C). SARS-CoV-2 infection significantly downregulated ETC genes 2 hours post-infection including *NDUFAB1*, a Complex I subunit which enhances the capacity and efficiency of mitochondrial energy metabolism by coordinating the assembly of ETC Complexes, and by regulating iron-sulfur biosynthesis and Complex I stability [52]. Also downregulated was *NDUFS7,* a nuclear-encoded, ETC Complex I subunit involved in megacomplex assembly [53]. Likewise *NDUFS8,* which is involved in ETC Complex I electron transfer and assembly [54] was downregulated. Genes relevant to bioenergetics and ATP synthesis were also significantly downregulated within 2 hours of SARS-CoV-2 infection (Fig. 1A, Table 2). Examples of downregulated bioenergetic genes include *PDHB*, a component of pyruvate dehydrogenase (PDH), the enzyme that catalyzes the conversion of pyruvate to acetyl-CoA. PDHB regulates glucose oxidation during pathologic conditions, such as cardiac hypertrophy [55]; but its role in viral infections remains uncertain. Also downregulated were *ATP5F1b* and *ATP5B* genes, which encode subunits of mitochondrial ATP synthase. Consistent with the downregulation of ETC and metabolic genes caused by SARS-CoV-2 infection, transduction with SARS-CoV-2 proteins or infection with HCoV-OC43 or MHV-1 decreased oxidative metabolism and ETC Complex I function in human AEC (Supplemental Fig. 5, Fig. 4B, and Supplemental Fig. 7, respectively). For example, SARS-CoV-2 protein Nsp7 inhibited oxidative metabolism and reduced Complex I activity (Supplemental Fig. 5). Likewise, HCoV-OC43 infection impaired basal OCR and reduced maximal respiration while also inhibiting ETC Complex I activity and lowering ATP concentrations in AEC (Fig. 4B). Thus, bioenergetic impairment and impaired ETC Complex I activity are conserved consequences of coronavirus-mitochondriopathy.

Consistent with our study, Gordon et al. identified SARS-CoV-2 proteins that regulate mitochondrial GO pathways that are potentially relevant to O_2-sensing and lung injury. These GO pathways include: *mitochondria* (regulated by Nsp4, Nsp8, Orf9c), *electron transport* (regulated by Nsp7, Orf9c), *regulation of ER morphology and the mitochondrial matrix and metabolism* (regulated by M), *protein trafficking into the ER and mitochondria* (regulated by Nsp5), and *vesicle trafficking* (regulated by Nsp7) [17]. They showed that Nsp4, Nsp8, Nsp7, Orf9c and M proteins interact with mitochondrial proteins, including metabolic enzymes, mitochondrial ribosomal targets and co-factors of iron-sulfur complexes relevant to ETC Complex I. Consistent with these viral proteins localizing to mitochondria we show transduced M protein on the mitochondrial surface, external to the matrix (Supplemental Fig. 6E); a finding we also made with HCoV-OC43 infection (Fig. 4Aviii).

4.3. Mitochondrial fission

Replicating SARS-CoV-2 and HCoV-OC43 caused mitochondrial fission (Figs. 3 and 4C, and Supplemental Figs. 4A–B) in both AEC and HPAEC. TEM revealed that HCoV-OC43 infection causes mitochondrial swelling, consistent with mitochondrial depolarization and pathologic mitochondrial fission (Fig. 4Bvii-ix). At 2 hours post-infection we observed upregulation of *DNM1L,* the gene encoding Drp1, a large GTPase which is the major mediator of mitochondrial fission. Consistent with this, SARS-CoV-2 infection increased the expression of both total

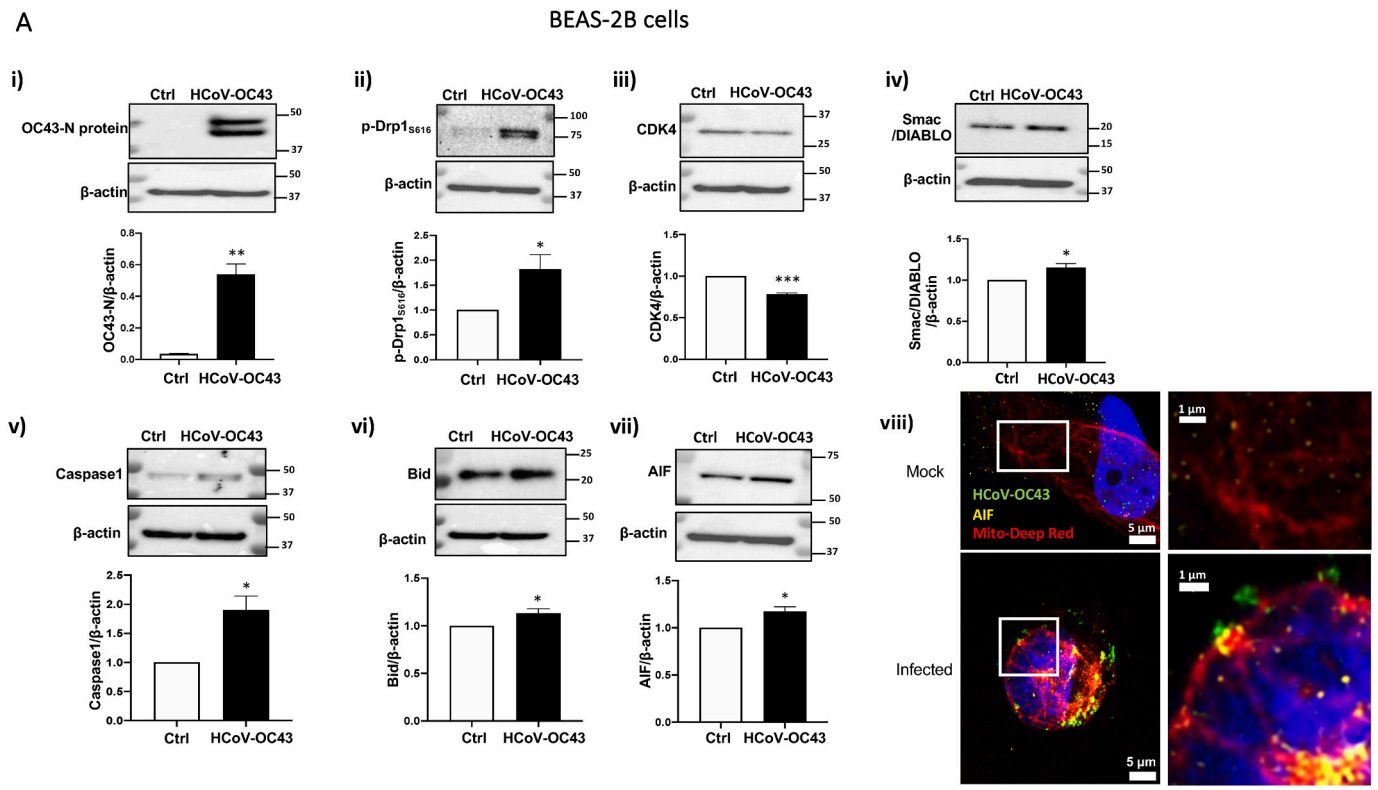

Fig. 4. HCoV-OC43 infection increases expression of apoptosis mediators and reduces oxidative metabolism in BEAS-2B cells and causes mitochondrial fission in HPAEC. Assessment of the effects of HCoV-OC43 infection of BEAS-2B cells and HPAEC occurred at 72 hours post infection.
A) HCoV-OC43 infection increases expression of apoptosis and mitochondrial fission mediators in BEAS-2B cells. Representative immunoblots and densitometry **i)** confirming infection with HCoV-OC43 (inset showing viral N-protein only in infected cells). Infection of human AEC upregulates **ii)** mediators of mitochondrial fission (total and activated Drp1, p-Drp1$_{S616}$). **iii)** downregulates CDK4, a cyclin dependent kinase responsible for cell cycle progression. **iv-vii)** upregulates apoptosis mediators (Smac/DIABLO, Caspase 1, Bid, and AIF). *$P < 0.05$; **$P < 0.01$; ***$P < 0.001$; n = 3/group.**viii)** Using STED microscopy at 50 nm resolution, coronavirus HCov-OC43 (green; nucleoprotein-targeted antibody) colocalizes with AIF (yellow) on the mitochondrial outer membrane (red) in AEC; AIF expression is also increased in infected cells (bottom) versus mock cells in these images (top), as in the immunoblot (vii). Scale bar = 1–5 μm
B) HCoV-OC43 infection inhibits oxidative metabolism and increases mitochondrial fission in BEAS-2B cells **i-iv)** Infection of human AEC with HCoV-OC43, inhibits basal and FCCP-stimulated maximal respiration and ATP-linked OCR, as measured by micropolarimetry. *$P < 0.05$; n = 5/group. v) Infection with HCoV-OC43 reduces ATP concentration in BEAS-2B cells. *$P < 0.05$; n = 9/group. **vi)** Infection with HCoV-OC43 inhibits ETC Complex I activity in BEAS-2B cells. ***$P < 0.001$; n = 5/group. **vii-viii)** TEM shows that mitochondria in infected cells are more swollen with increased intercristal space. ****$P < 0.0001$; n = 39 mitochondria/group. **ix)** TEM shows HCoV-OC43 virus in an intracellular vesicle.
C) HCoV-OC43 fragments mitochondria in HPAEC. Infection of HPAEC with HCoV-OC43 causes mitochondrial fission (more punctate mitochondria in infected cells on right vs control cells on left). The mitochondrial network is red (loaded with the potentiometric dye tetra methylrhodamine, TMRM). We used machine

and activated Drp1 and greatly increased the ratio of activated/total enzyme at 72 hours (Fig. 3F). Likewise, HCoV-OC43 increased the expression of activated Drp1 (p-Drp1$_{S616}$) in AEC (Fig. 4Aii) and produced mitochondrial fission in HPAEC (Fig. 4C, Supplemental Fig. 4), suggesting that mitochondrial fission is another conserved hallmark of coronavirus-mitochondriopathy. The SARS-CoV-2 proteins Nsp7 and Nsp9 recapitulated the pro-fission effects of replicating coronavirus (Supplemental Fig. 3). While we did not study the consequences of mitochondrial fission in this study, it can contribute to cell death by several mechanisms, including increasing production of mitochondrial-derived ROS [56].

4.4. Heterogeneity in the effects of individual SARS-CoV-2 proteins

Many aspects of coronavirus-induced mitochondriopathy were recapitulated by transduction with single SARS-CoV-2 proteins, which we interpret as evidence that SARS-CoV-2 mitochondriopathy can occur independent of inflammation, likely by protein-protein interaction, as shown by Ramachandran [13]. Some aspects of the mitochondriopathy (including apoptosis and increased Drp1 expression) were induced by each of the viral proteins we tested. However, as would be expected if specific protein-protein interactions occur between SARS-CoV-2 proteins and host mitochondrial proteins, we observed heterogeneity in the effects of SARS-CoV-2 proteins on some mitochondrial functions, including O_2-sensing, metabolism, mitochondrial fission, and cell cycle progression. For example, only M and Nsp9 proteins significantly inhibited HPV (Fig. 6), only Nsp7 and Nsp9 promoted mitochondrial fission (Supplemental Fig. 3A), only Nsp7 impaired mitochondrial oxidative metabolism (Supplemental Fig. 5) and only M protein caused cell cycle arrest (Fig. 5D), reduced mPTP activity (Fig. 5E) and activated caspase 7 (Supplemental Fig. 3B). These protein-specific interactions point toward the mechanisms underlying various aspects of the viral mitochondriopathy and may also represent new therapeutic targets.

4.5. Hypoxic pulmonary vasoconstriction

We observed that specific SARS-CoV-2 proteins, Nsp9 and M selectively suppressed HPV in human PASMC, without altering the response

learning to allow a computer algorithm to classify mitochondria as punctate, intermediate, or filamentous, as described [31]. Infection increases the percentage area of intermediate and punctate mitochondria, consistent with induction of mitochondrial fission. $^{**}P < 0.01$, $^{****}P < 0.0001$; n = 20 cells/group.

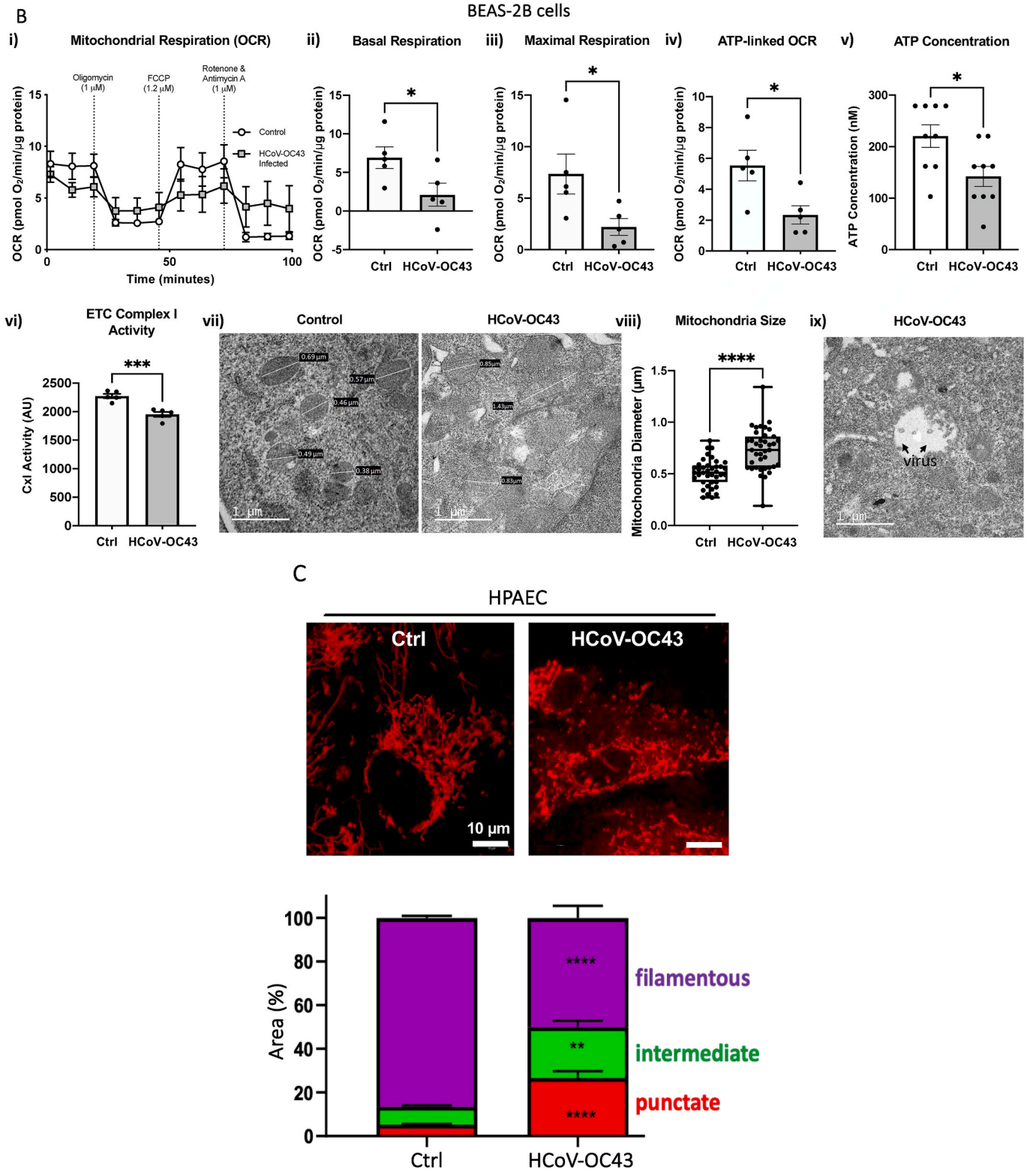

Fig. 4. (*continued*).

to KCl, indicating they are interfering with oxygen-sensing rather than impairing PASMC contractility (Fig. 6). The observation that heterologously expressed SARS-CoV-2 proteins suppress HPV in human PASMC suggests this effect can result from direct protein-protein interaction, without an obligatory requirement for an inflammatory milieu (Fig. 6). HPV was also largely eliminated in the MHV-1 pneumonia model, and this was associated with severe hypoxemia (Fig. 7Ci). These *in vivo* experiments support the interpretation that impaired HPV contributes to hypoxemia in coronavirus pneumonia. Bay K8644, which enhanced HPV, an effect previously shown to be due to its ability to increase the

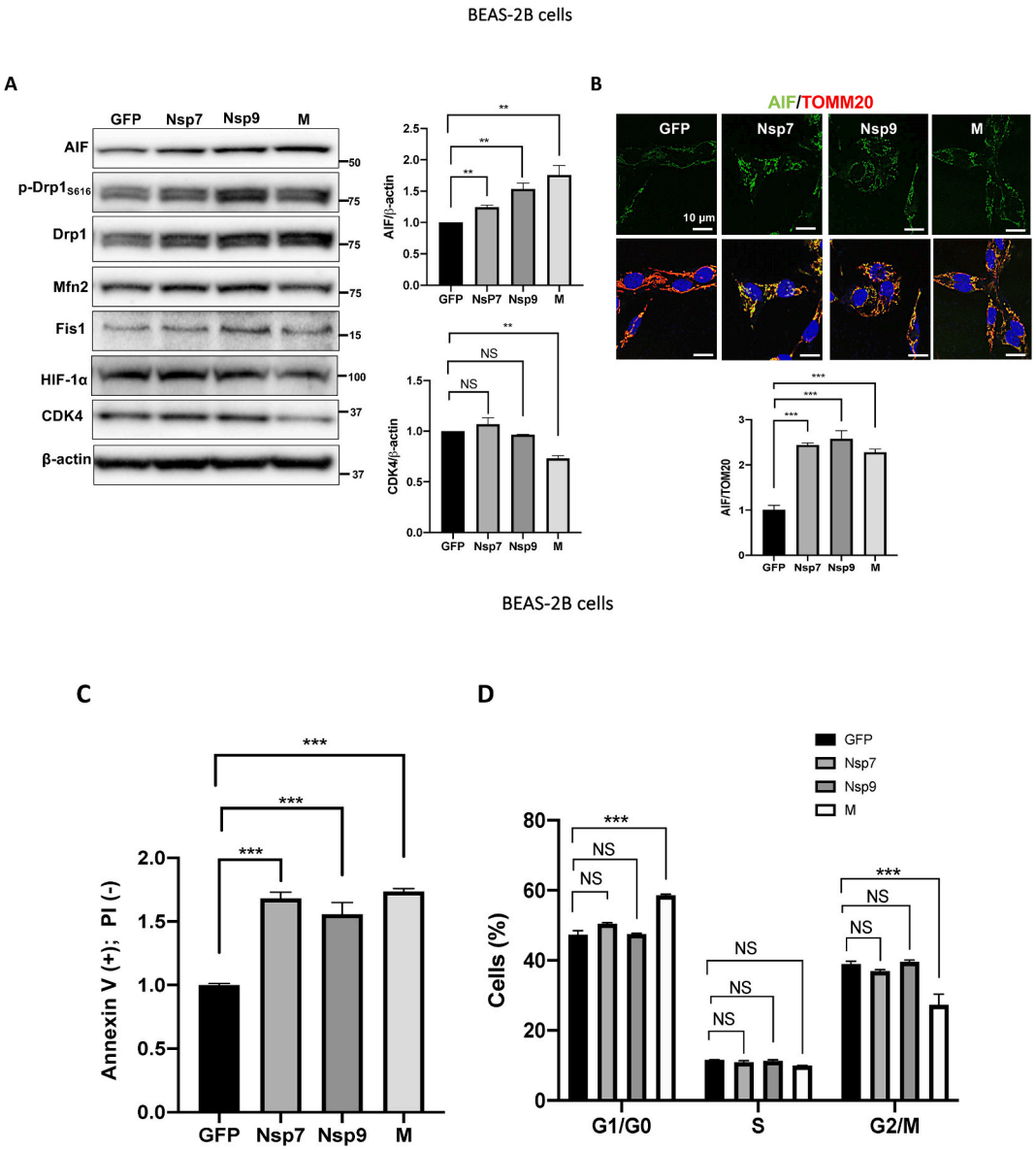

Fig. 5. Transduction with SARS-CoV-2 proteins increases apoptosis and causes cell cycle arrest in BEAS-2B cells.

A) Representative immunoblots and densitometry showing upregulated expression of AIF and CDK4, 96 hours following transduction with 3 different SARS-CoV-2 proteins (vs GFP control). Only transduction with M protein downregulates CDK4. $^{**}P < 0.01$; NS, not significant; n = 3/group.

B) Representative images and mean data showing that heterologous expression of each of the three selected SARS-CoV-2 proteins increase the expression of AIF relative to the mitochondrial reporter protein, TOMM20, in BEAS-2B cells at 96 hours. Cells were stained with AIF mouse monoclonal antibody (green). Cells were also stained with TOMM20 rabbit polyclonal antibody (red). Ex/Em: 556/560-580 nm $^{***}P < 0.001$; n = 5–7/group.

C) Lentiviral transduction of A549 cells with SARS-CoV-2 proteins, Nsp7, Nsp9 & M increase apoptosis, defined as cells that are annexin V positive and propidium iodide (PI) negative, relative to the GFP control. $^{***}P < 0.001$; n = 3/group.

D) Lentiviral transduction of A549 cells with SARS-CoV-2 M protein causes cell cycle arrest in G1/G0, relative to GFP controls and other SARS-CoV-2 proteins. $^{***}P < 0.001$; NS; not significant; n = 3/group.

E) BEAS-2B cells were loaded with mPTP staining dye-AM (Abcam ab239704; flow cytometry kit). $CoCl_2$ was used to quench the cytosolic fluorescence, maintaining only the mitochondrial signal. Histograms demonstrate reduced mPTP activity (as the result of the mPTP opening) in M-transfected cells (light gray) versus control (dotted histogram). mPTP activity was not affected in Nsp9-transfected cells (dark gray) compared to control. The bar graph shows the fold change comparison in mPTP activity and confirms that that M-transfected cells had significantly reduced mPTP activity (open mPTP) versus control ($p = 0.019$; parametric one-way ANOVA). mPTP activity was calculated as MFI($CoCl_2$) – MFI ($CoCl_2$+Ionomycin); MFI – median fluorescence intensity. MFI = mean fluorescent intensity. $^{*}P < 0.05$; NS; not significant; n = 4/group.

open state probability of L-type calcium channels in PASMC [35], also improved systemic oxygenation (Fig. 7Ciii), presumably by correcting V/Q mismatch.

The mechanism of HPV involves O_2-sensitive variation in the production of ROS by NDUFS2 in ETC Complex I [18]. These ETC Complex I-derived ROS serve as diffusible signaling molecules and regulate vascular tone through redox regulation of ion channels and enzymes, reviewed in [7]. While Gordon et al. did not report

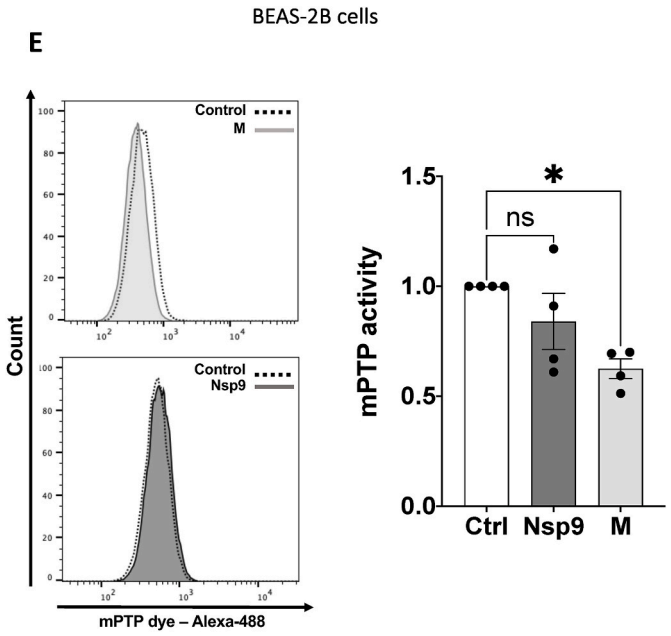

Fig. 5. (*continued*).

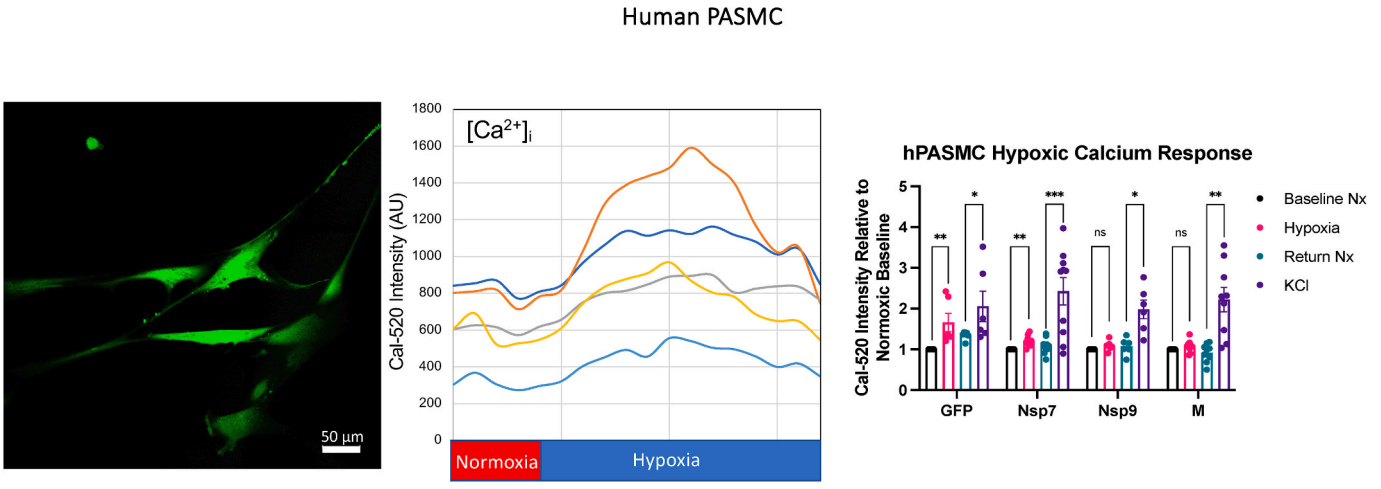

Fig. 6. SARS-CoV-2 proteins inhibit HPV in human PASMC. In the representative trace (left) a control hypoxic response is shown. Note that the rapid rise in $[Ca^{2+}]_i$ in human PASMC, a surrogate for HPV. Note the loss of a significant hypoxic increases in $[Ca^{2+}]_i$ (pink bar in graph) caused by transduction with M or Nsp9 SARS-CoV-2 viral proteins. Transduction with lentiviral GFP served as the control. Also note none of the SARS-CoV-2 proteins altered the KCl-induced rise in $[Ca^{2+}]_i$ (purple). $^*P < 0.05$, $^{**}P < 0.01$, $^{***}P < 0.001$, NS; not significant; n = 6–10 cells/group.

SARS-CoV-2 protein interactions with NDUFS2, they identified other interacting mitochondrial proteins relevant to ETC Complex I stability and function. For example, Nsp7 interacts with NDUFAF2, a molecular chaperone for Complex I assembly [17], and Orf9c interacts with NDUFAF1, which is also important for ETC Complex I assembly [17]. NDUFAF2 deficiency increases oxidative stress, causes mitochondrial DNA depletion, and is associated with reduced Complex I activity [57]. Orf9c also interacts with NDUFB9, a noncatalytic, accessory factor within Complex I [58]. Thus, SARS-CoV-2 is well-positioned to interfere with ETC Complex I function, and we did observe impaired Complex I function following HCoV-OC43 infection (Fig. 4Bvi) and transduction with Nsp7 (Supplemental Fig. 5C). Moreover, SARS-CoV-2 infection altered the expression of many genes involved in the assembly and function of ETC Complex I (Supplemental File 1), which likely contributes to the impaired O_2-sensing and reduced ETC Complex I activity we observed. Further work will be required to assess the contribution of the transcriptomic changes we identified in *NDUFAB1*, *NDUFS7*, and *NDUFS8* (Table 2) to the observed impairment of ETC Complex I function.

Our finding of impaired HPV corroborates the observation of Caravita et al. who studied 21 mechanically ventilated COVID-19 pneumonia patients versus 21 dyspneic control subjects and confirmed the absence of HPV using right heart catheterization [59]. These COVID-19 patients had mildly elevated left heart filling pressures but normal pulmonary vascular resistance, indicating that their pulmonary hypertension reflected mild left heart disease. They concluded that impaired HPV, as we proposed in 2020 [5], coupled with mildly elevated left heart diastolic pressures [59], promotes capillary engorgement and lung edema which exacerbates COVID-19 pneumonia [5,59].

Mitochondrial pathways have not yet been exploited as therapeutic

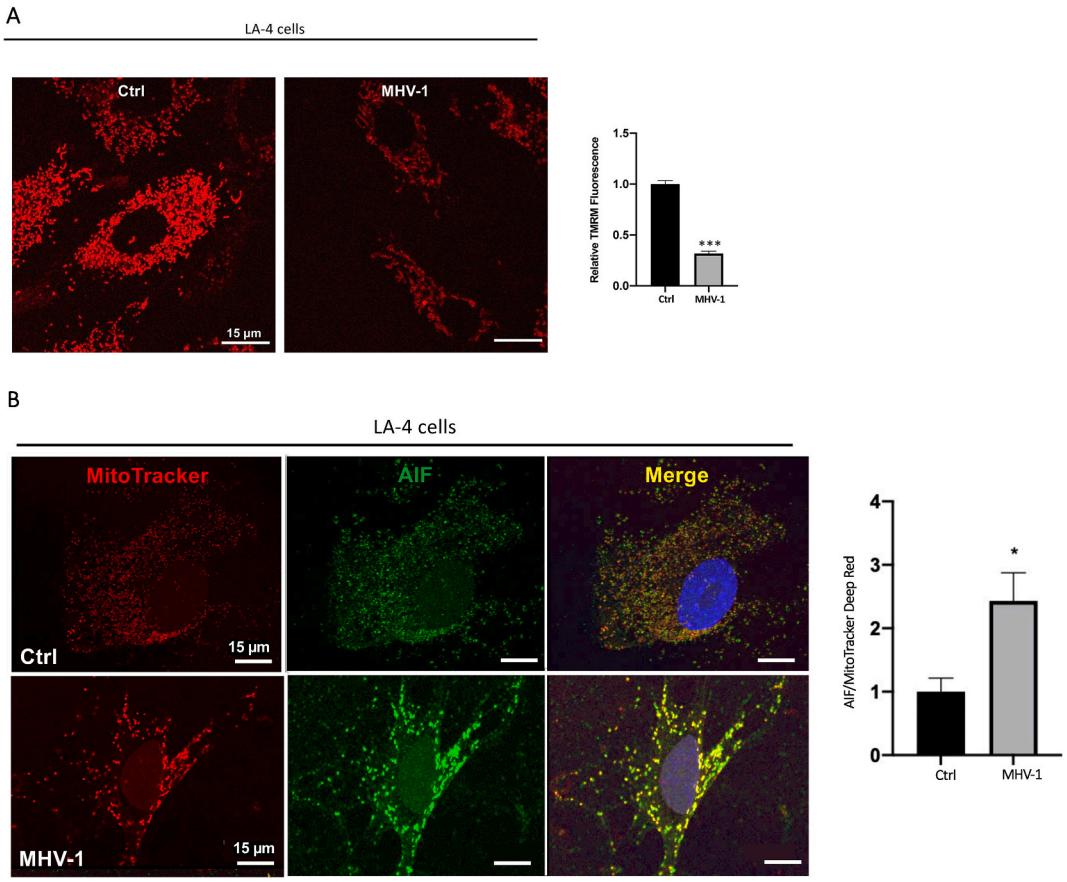

Fig. 7. MHV-1 causes a mitochondriopathy that increases apoptosis and suppresses HPV.

A) MHV-1 reduces ΔΨm in murine cells. Mitochondria in LA-4 adenoma cells are seen in red, reflecting their uptake of TMRM, a potentiometric dye. MHV-1 reduced relative TMRM fluorescence, which is interpreted as a relative depolarization of ΔΨm **(Supplemental Fig. 6); measured 96 hours after infection. ***$P<0.001$; n=15 cells/group.**

B) MHV-1 infection upregulates AIF expression in mitochondria and causes nuclear translocation of AIF in murine cells. LA-4 murine adenoma cells were infected with MHV-1(0.05 pfu/cell) for 96 hours. Cells were immunostained for AIF (green) and loaded with MitoTracker Deep Red (Invitrogen, 150 nM) for 1 hour at 37°C. The cells were also stained with DAPI to identify the nuclei (blue). Cells were imaged at Ex/Em: 644/655–675. Note the increase in AIF, both in mitochondria and in the nucleus. *$P<0.05$; n=4–6 cells/group.

C) MHV-1 pneumonia induces hypoxemia, inhibits HPV, and increases AEC apoptosis.

i) Male and female A/J mice develop systemic oxygen desaturation with MHV-1 infection at days 4–6. (n=4 for male Ctrl, n=4 for male MHV-1, n=5 for female Ctrl, n=3 for female MHV-1)

ii) Representative RV pressure traces and mean data show that HPV is suppressed in MHV-1 mice. There was no significant increase in RV systolic pressure with hypoxia in MHV-1 infected mice, in contrast to the robust rise (HPV) in uninfected mice. Note that IP treatment with Bay K8644 significantly augmented HPV (defined as the Δ RVSP in response to hypoxia) in both control and infected mice. (n=8 for Ctrl, n=7 for MHV-1)

iii) Bay K8644 (1 mg/kg IP) increases O_2 saturation. (n=9 for Ctrl, n=7 for MHV-1). The higher O_2 saturations in this panel (vs panel i) reflect the animals were being mechanically ventilated with room air (versus spontaneous breathing of room air in panel i).

iv) Micro-CT images acquired using a VECTor [4]CT scanner. The CT scans show lung consolidation in MHV-1 mice (on right). The histology insets show inflammatory infiltrates in the MHV-1 lung. Histology could not be performed on the same lungs as the CT scan, because the CT scans were done with barium infusion.

v) Immunofluorescent staining of MHV-Nsp9 protein and TUNEL assay show colocalization of Nsp9 and TUNEL in MHV-1 infected lungs. This illustrates that only infected AEC developed apoptosis.

The bar graph quantifies MHV-1 induced apoptosis, identified by (+) TUNEL green stain within AEC nuclei (in panel iv inset) (n=9 for Ctrl, n=9 for MHV-1). *$P<0.05$, **$P<0.01$, ***$P<0.001$.

targets for COVID-19. However, mitochondrial apoptosis, induced in human neurons by West Nile virus (also an RNA virus), is inhibited by the antibiotic minocycline [60]. Minocycline not only prevents viral-induced apoptosis but also reduces viral titers, although this is not necessarily a rigorous surrogate of benefit in infected patients [60]. We speculate that anti-apoptotic, mitochondrial-targeted therapies might prevent cell death and reduce viral spread. However, the role of apoptosis in viral infections is complex and it may be protective in some circumstances [61]. Augmenting HPV also has potential as a therapeutic strategy for countering hypoxemia in COVID-19 pneumonia patients. Candidate drugs for repurposing for short term enhancement of HPV, after being tested in clinical trials, include the respiratory stimulant, almitrine [62], the prostaglandin synthase inhibitor, indomethacin [63] and methylene blue (a guanylate cyclase inhibitor).

5. Limitations

This study has several limitations. First, we did not directly study mitochondria in the lungs of patients with COVID-19 pneumonia. Second, we did not determine the extent to which mitochondrial damage

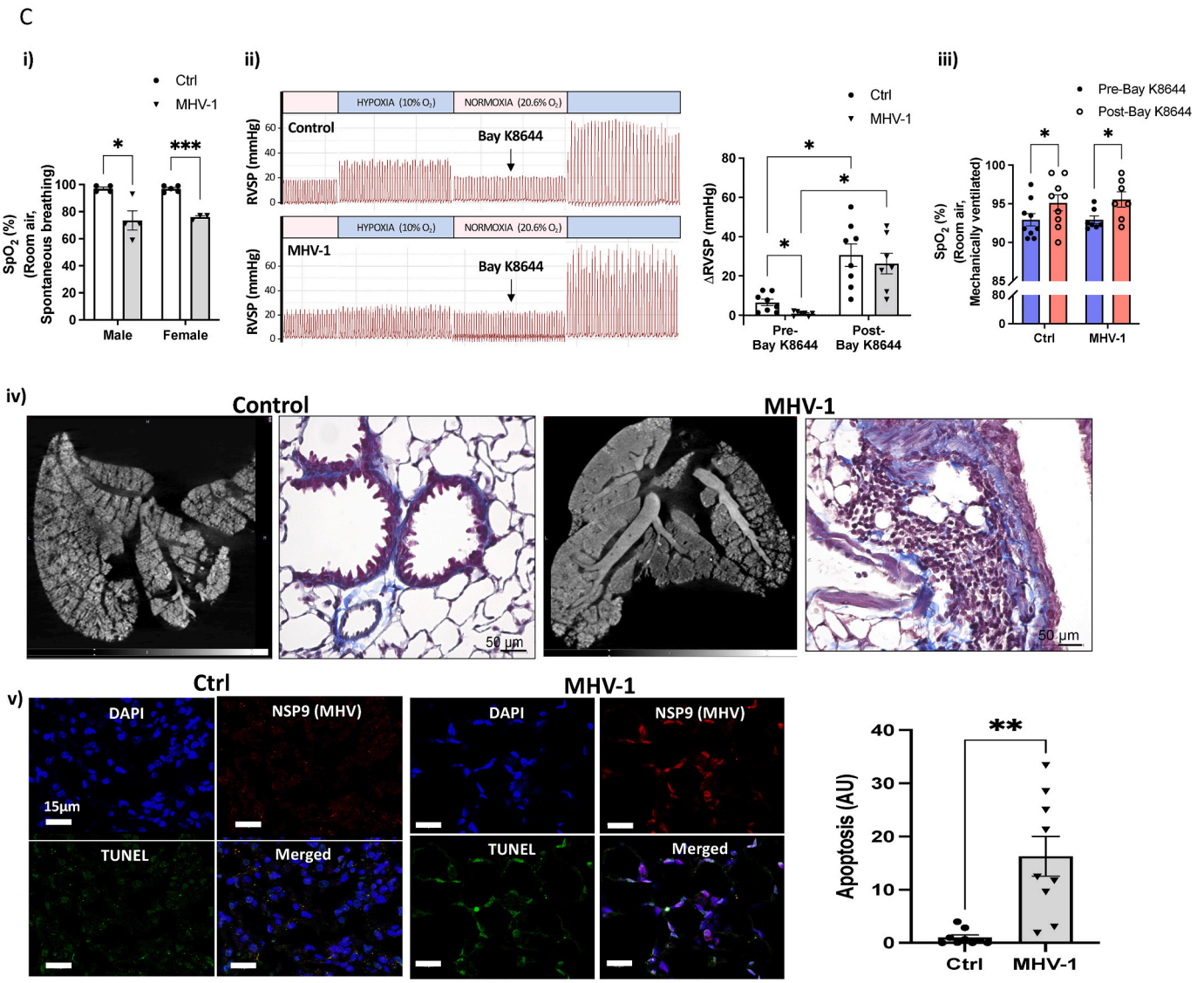

Fig. 7. (*continued*).

might reflect mechanisms involving inflammation or activation of the innate immune system [64]. This is important because SARS-CoV-2 causes inflammation with production of proinflammatory cytokines and chemokines [64]. Third, while we demonstrate bioenergetic impairment and excessive mitochondrial fission result from SARS-CoV-2 and other coronaviruses, the impact of these abnormalities on the pathogenesis of COVID-19 pneumonia requires further study. While it is tempting to speculate such bioenergetic changes could contribute to the long COVID-19 syndrome this will require direct experimental evaluation. Finally while much of this study used SARS-CoV-2 virus or SARS-CoV-2 viral proteins we also rely on HCoV-OC43 infections to reinforce our conclusions. A Clustal amino acid sequence alignment shows that the amino acid sequence homology between the Nsp7, Nsp9 and M proteins of HCoV-OC43 and SARS-CoV-2's is limited (50%, 45% and 40%, respectively). Nonetheless, a practical advantage of doing some studies with HCoV-OC43 is that it only requires CL2 biocontainment, which accelerates research. Moreover, we primarily use HCoV-OC43 because it is an established cause of pneumonia in adults and children and is from the same betacoronavirus family as SARS-CoV-2.

6. Conclusion

We show that SARS-CoV-2, transduced SARS-CoV-2 proteins, HCoV-OC43 and MHV-1 induce apoptosis, mitochondrial fission and bioenergetic impairment in AEC and interfere with mitochondria O_2-sensing in PASMC. Viral-induced mitochondrial damage exacerbates lung injury and impairs HPV, likely contributing to the profound hypoxemia of COVID-19 pneumonia patients, as schematically outlined in Fig. 8. This coronavirus-induced mitochondriopathy is potentially relevant to the pathophysiology of COVID-19 pneumonia and may offer novel therapeutic targets, including the development of drugs that inhibit mitochondrial-mediated apoptosis and mitochondrial fission, as well as repurposing agents that enhance HPV.

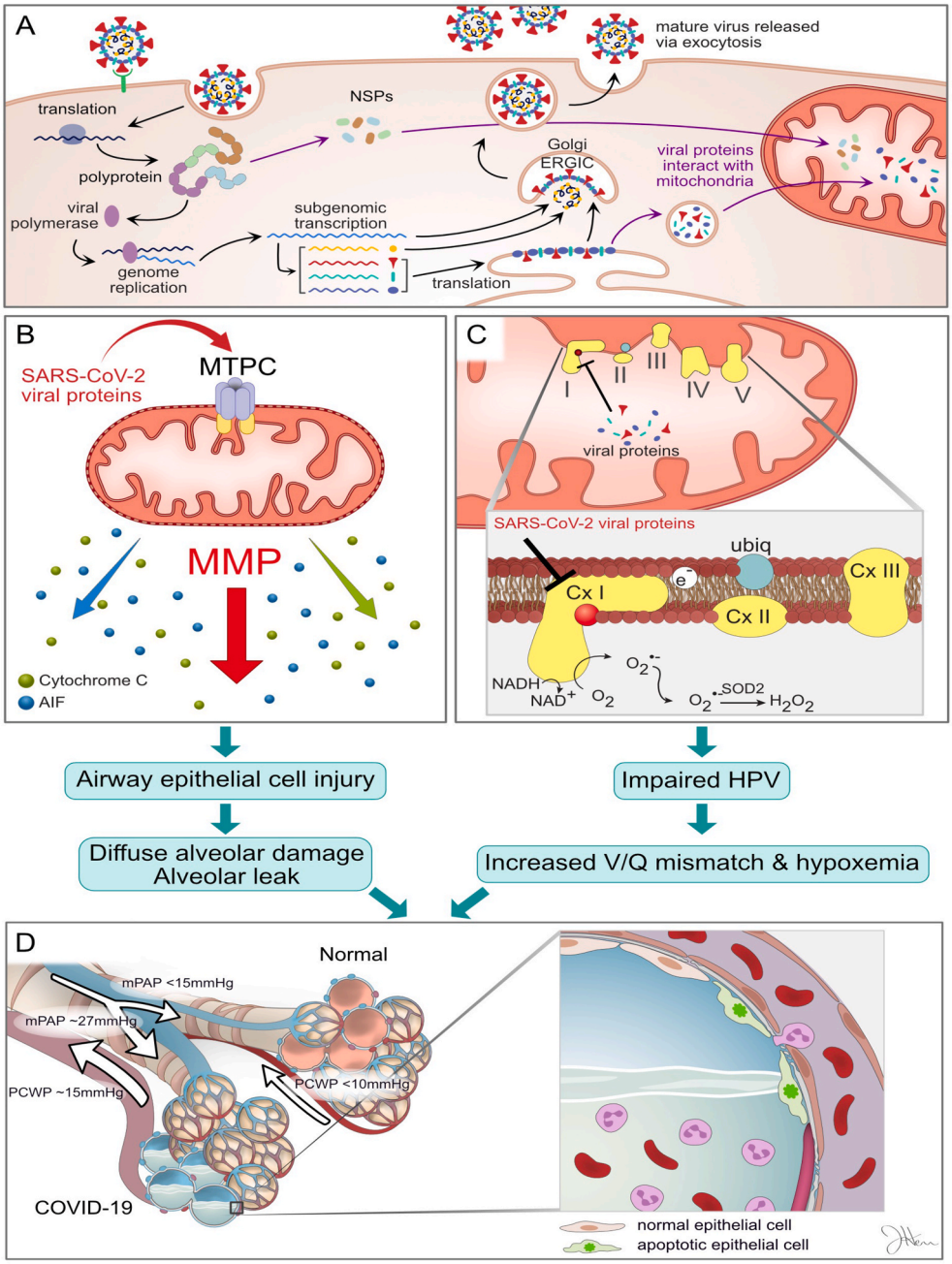

Fig. 8. Proposed mechanism by which SARS-CoV-2 mitochondriopathy contributes to COVID-19 pneumonia. SARS-CoV-2 mitochondriopathy causes DAD and hypoxemia in part by inducing apoptosis (left) and by suppressing HPV (right).
A) Viral replication floods the cell with viral proteins.
B) In airway epithelial cells some viral proteins target the mitochondria transition pore complex (MTPC) which permeabilizes the membrane (MMP) and leads to leak of apoptosis mediators, like AIF and cytochrome *c*, resulting in apoptosis.
C) In PASMC viral proteins interact with components of ETC Complex I, the site of O_2-sensing, and impair HPV.
D) The consequences of this mitochondriopathy include impaired HPV, which inappropriately floods capillaries in infected segments with blood, exacerbating capillary leak and promoting V/Q mismatch. Excessive apoptosis damages the alveoli and contributes to DAD. The loss of HPV combined with AEC apoptosis exacerbate systemic hypoxemia in coronavirus pneumonia syndromes, including COVID-19 pneumonia. In addition, there is profound mitochondrial fission and bioenergetic impairment which contribute to the lung injury (not shown in this figure).

Declaration of competing interest

None.

Acknowledgements

This work was funded by the Canadian Institutes for Health Research (CIHR) Foundation Grant (SLA), National Institutes of Health R01-HL071115 (SLA), 1RC1HL099462 (SLA), the William J. Henderson Foundation (SLA), and a grant from the Southeastern Ontario Medical Association (SEAMO, SLA). This work was also supported by the Canada Research Chairs Program (Tier II, KDS), the Canada Foundation for Innovation (CFI) – John R. Evans Leaders Fund (KDS), the Banting Research Foundation – Mitacs (KDS and CCC), and Research Initiation Grants from Queen's University (KDS and CCC). VIDO receives operational funding from the Government of Saskatchewan through Innovation Saskatchewan and the Ministry of Agriculture, and from the CFI – Major Science Initiatives for its CL3 facility. This work is also supported by the Natural Sciences and Engineering Research Council of Canada (CCC). Dr. Archer gratefully acknowledges the contributions of the late Dr. Victor Snieckus, Department of Chemistry, Queen's University who advised on matters related to discovery chemistry for treating COVID-19. He also thanks Dr. Mark Ormiston for the generous gift of human pulmonary artery endothelial cells (HPAEC) used in these studies.

Appendix A. Supplementary data

Supplementary data to this article can be found online at https://doi.org/10.1016/j.redox.2022.102508.

References

[1] W.J. Guan, Z.Y. Ni, Y. Hu, et al., Clinical characteristics of coronavirus disease 2019 in China, N. Engl. J. Med. 382 (2020) 1708–1720.
[2] COVID-19 Resources: Canadian Outbreak At-A-Glance, 2022 at, https://resources-covid19canada.hub.arcgis.com.
[3] S.E. Fox, A. Akmatbekov, J.L. Harbert, G. Li, J. Quincy Brown, R.S. Vander Heide, Pulmonary and cardiac pathology in African American patients with COVID-19: an autopsy series from New Orleans, Lancet Respir. Med. 8 (2020) 681–686.
[4] L. Gattinoni, S. Coppola, M. Cressoni, M. Busana, D. Chiumello, Covid-19 does not lead to a "typical" acute respiratory distress syndrome, Am. J. Respir. Crit. Care Med. 201 (2020) 1299–1300.
[5] S.L. Archer, W.W. Sharp, E.K. Weir, Differentiating COVID-19 pneumonia from acute respiratory distress syndrome (ARDS) and high altitude pulmonary edema (HAPE): therapeutic implications, Circulation 142 (2020) 101–104.
[6] X. Cao, M. Fu, R. Bi, et al., Cadmium induced BEAS-2B cells apoptosis and mitochondria damage via MAPK signaling pathway, Chemosphere 263 (2021), 128346.
[7] E.K. Weir, J. Lopez-Barneo, K.J. Buckler, S.L. Archer, Acute oxygen-sensing mechanisms, N. Engl. J. Med. 353 (2005) 2042–2055.
[8] H. Yan, G. Xiao, J. Zhang, et al., SARS coronavirus induces apoptosis in Vero E6 cells, J. Med. Virol. 73 (2004) 323–331.
[9] L. Zhang, L. Wei, D. Jiang, J. Wang, X. Cong, R. Fei, SARS-CoV nucleocapsid protein induced apoptosis of COS-1 mediated by the mitochondrial pathway, Artif. Cells Blood Substit. Immobil. Biotechno. 35 (2007) 237–253.
[10] H. Everett, G. McFadden, Viruses and apoptosis: meddling with mitochondria, Virology 288 (2001) 1–7.
[11] S. Neumann, S. El Maadidi, L. Faletti, et al., How do viruses control mitochondria-mediated apoptosis? Virus Res. 209 (2015) 45–55.
[12] L. Galluzzi, C. Brenner, E. Morselli, Z. Touat, G. Kroemer, Viral control of mitochondrial apoptosis, PLoS Pathog. 4 (2008), e1000018.
[13] K. Ramachandran, S. Maity, A.R. Muthukumar, et al., SARS-CoV-2 infection enhances mitochondrial PTP complex activity to perturb cardiac energetics, iScience 25 (2022), 103722.
[14] S. Landshamer, M. Hoehn, N. Barth, et al., Bid-induced release of AIF from mitochondria causes immediate neuronal cell death, Cell Death Differ. 15 (2008) 1553–1563.
[15] C. Wang, R.J. Youle, The role of mitochondria in apoptosis, Annu. Rev. Genet. 43 (2009) 95–118.
[16] C.C. Lai, M.J. Jou, S.Y. Huang, et al., Proteomic analysis of up-regulated proteins in human promonocyte cells expressing severe acute respiratory syndrome coronavirus 3C-like protease, Proteomics 7 (2007) 1446–1460.
[17] D.E. Gordon, G.M. Jang, M. Bouhaddou, et al., A SARS-CoV-2 protein interaction map reveals targets for drug repurposing, Nature 583 (2020) 459–468.
[18] K.J. Dunham-Snary, D. Wu, F. Potus, et al., Ndufs2, a core subunit of mitochondrial complex I, is essential for acute oxygen-sensing and hypoxic pulmonary vasoconstriction, Circ. Res. 124 (2019) 1727–1746.
[19] A. Jean, C. Quach, A. Yung, M. Semret, Severity and outcome associated with human coronavirus OC43 infections among children, Pediatr. Infect. Dis. J. 32 (2013) 325–329.
[20] J. Reina, C. Lopez-Causape, E. Rojo-Molinero, R. Rubio, Clinico-epidemiological characteristics of acute respiratory infections caused by coronavirus OC43, NL63 and 229E, Rev. Clin. Esp. 214 (2014) 499–504.
[21] D.M. Patrick, M. Petric, D.M. Skowronski, et al., An outbreak of human coronavirus OC43 infection and serological cross-reactivity with SARS coronavirus, Can. J. Infect Dis. Med. Microbiol. 17 (2006) 330–336.
[22] S. Provencher, S.L. Archer, F.D. Ramirez, et al., Standards and methodological rigor in pulmonary arterial hypertension preclinical and translational research, Circ. Res. 122 (2018) 1021–1032.
[23] Z. Yang, J. Du, G. Chen, et al., Coronavirus MHV-A59 infects the lung and causes severe pneumonia in C57BL/6 mice, Virol. Sin. 29 (2014) 393–402.
[24] N. De Albuquerque, E. Baig, X. Ma, et al., Murine hepatitis virus strain 1 produces a clinically relevant model of severe acute respiratory syndrome in A/J mice, J. Virol. 80 (2006) 10382–10394.
[25] J.A. Aguiar, B.J. Tremblay, M.J. Mansfield, et al., Gene expression and in situ protein profiling of candidate SARS-CoV-2 receptors in human airway epithelial cells and lung tissue, Eur. Respir. J. 56 (2020).
[26] A. Banerjee, N. El-Sayes, P. Budylowski, et al., Experimental and natural evidence of SARS-CoV-2-infection-induced activation of type I interferon responses, iScience 24 (2021), 102477.
[27] A. Banerjee, J.A. Nasir, P. Budylowski, et al., Isolation, sequence, infectivity, and replication kinetics of severe acute respiratory syndrome coronavirus 2, Emerg. Infect. Dis. 26 (2020) 2054–2063.
[28] M.I. Love, W. Huber, S. Anders, Moderated estimation of fold change and dispersion for RNA-seq data with DESeq2, Genome Biol. 15 (2014) 550.
[29] G. Yu, L.G. Wang, Y. Han, Q.Y. He, clusterProfiler: an R package for comparing biological themes among gene clusters, OMICS 16 (2012) 284–287.
[30] K.H. Chen, A. Dasgupta, J. Lin, et al., Epigenetic dysregulation of the dynamin-related protein 1 binding partners MiD49 and MiD51 increases mitotic mitochondrial fission and promotes pulmonary arterial hypertension: mechanistic and therapeutic implications, Circulation 138 (2018) 287–304.
[31] D. Wu, A. Dasgupta, K.H. Chen, et al., Identification of novel dynamin-related protein 1 (Drp1) GTPase inhibitors: therapeutic potential of Drpitor1 and Drpitor1a in cancer and cardiac ischemia-reperfusion injury, Faseb. J. 34 (2020) 1447–1464.
[32] F. Potus, A.Y. Martin, B. Snetsinger, S.L. Archer, Biventricular assessment of cardiac function and pressure-volume loops by closed-chest catheterization in mice, J Vis Exp (160) (2020).
[33] S.L. Archer, J.P. Tolins, L. Raij, E.K. Weir, Hypoxic pulmonary vasoconstriction is enhanced by inhibition of the synthesis of an endothelium derived relaxing factor, Biochem. Biophys. Res. Commun. 164 (1989) 1198–1205.
[34] R.D. Cardiff, C.H. Miller, R.J. Munn, Manual hematoxylin and eosin staining of mouse tissue sections, Cold Spring Harb. Protoc. 2014 (2014) 655–658.
[35] M. Tolins, E.K. Weir, E. Chesler, D.P. Nelson, A.H. From, Pulmonary vascular tone is increased by a voltage-dependent calcium channel potentiator, J. Appl. Physiol. 60 (1985) 942–948.
[36] S. Luo, D.C. Rubinsztein, BCL2L11/BIM: a novel molecular link between autophagy and apoptosis, Autophagy 9 (2013) 104–105.
[37] M. Magni, G. Buscemi, L. Zannini, Cell cycle and apoptosis regulator 2 at the interface between DNA damage response and cell physiology, Mutat. Res. Rev. Mutat. Res. 776 (2018) 1–9.
[38] Y. Cheng, W. Luo, Z. Li, et al., CircRNA-012091/PPP1R13B-mediated lung fibrotic response in silicosis via endoplasmic reticulum stress and autophagy, Am. J. Respir. Cell Mol. Biol. 61 (2019) 380–391.
[39] E. Beurel, R.S. Jope, The paradoxical pro- and anti-apoptotic actions of GSK3 in the intrinsic and extrinsic apoptosis signaling pathways, Prog. Neurobiol. 79 (2006) 173–189.
[40] I. Guella, M.B. McKenzie, D.M. Evans, et al., De novo mutations in YWHAG cause early-onset epilepsy, Am. J. Hum. Genet. 101 (2017) 300–310.
[41] P. Wang, Y. Deng, X. Fu, MiR-509-5p suppresses the proliferation, migration, and invasion of non-small cell lung cancer by targeting YWHAG, Biochem. Biophys. Res. Commun. 482 (2017) 935–941.
[42] Q. Song, J. Song, Q. Wang, et al., miR-548d-3p/TP53BP2 axis regulates the proliferation and apoptosis of breast cancer cells, Cancer Med. 5 (2016) 315–324.
[43] K. Tsunekawa, F. Kondo, T. Okada, et al., Enhanced expression of WD repeat-containing protein 35 (WDR35) stimulated by domoic acid in rat hippocampus: involvement of reactive oxygen species generation and p38 mitogen-activated protein kinase activation, BMC Neurosci. 14 (2013) 4.
[44] Z. Liu, Q. Luo, C. Guo, Bim and VDAC1 are hierarchically essential for mitochondrial ATF2 mediated cell death, Cancer Cell Int. 15 (2015) 34.
[45] J.F. Chan, A.J. Zhang, S. Yuan, et al., Simulation of the clinical and pathological manifestations of Coronavirus Disease 2019 (COVID-19) in golden Syrian hamster model: implications for disease pathogenesis and transmissibility, Clin. Infect. Dis. 71 (2020) 2428–2446.
[46] E.A. Thompson, K. Cascino, A.A. Ordonez, et al., Metabolic programs define dysfunctional immune responses in severe COVID-19 patients, Cell Rep. 34 (2021), 108863.
[47] D. Scozzi, M. Cano, L. Ma, et al., Circulating mitochondrial DNA is an early indicator of severe illness and mortality from COVID-19, JCI Insight 6 (2021) e143299.
[48] Y. Yang, Y. Wu, X. Meng, et al., SARS-CoV-2 membrane protein causes the mitochondrial apoptosis and pulmonary edema via targeting BOK, Cell Death Differ. 29 (2022) 1395–1408.
[49] Y. Yang, Z. Xiong, S. Zhang, et al., Bcl-xL inhibits T-cell apoptosis induced by expression of SARS coronavirus E protein in the absence of growth factors, Biochem. J. 392 (2005) 135–143.
[50] D.J. Favreau, M. Meessen-Pinard, M. Desforges, P.J. Talbot, Human coronavirus-induced neuronal programmed cell death is cyclophilin d dependent and potentially caspase dispensable, J. Virol. 86 (2012) 81–93.
[51] Y. Liu, Y. Pu, X. Zhang, Role of the mitochondrial signaling pathway in murine coronavirus-induced oligodendrocyte apoptosis, J. Virol. 80 (2006) 395–403.
[52] T. Hou, R. Zhang, C. Jian, et al., NDUFAB1 confers cardio-protection by enhancing mitochondrial bioenergetics through coordination of respiratory complex and supercomplex assembly, Cell Res. 29 (2019) 754–766.
[53] V.F. Rhein, J. Carroll, S. Ding, I.M. Fearnley, J.E. Walker, NDUFAF5 hydroxylates NDUFS7 at an early stage in the assembly of human complex I, J. Biol. Chem. 291 (2016) 14851–14860.
[54] R. de Sury, P. Martinez, V. Procaccio, J. Lunardi, J.P. Issartel, Genomic structure of the human NDUFS8 gene coding for the iron-sulfur TYKY subunit of the mitochondrial NADH:ubiquinone oxidoreductase, Gene 215 (1998) 1–10.
[55] A. Mitra, T. Basak, S. Ahmad, et al., Comparative proteome profiling during cardiac hypertrophy and myocardial infarction reveals altered glucose oxidation by differential activation of pyruvate dehydrogenase E1 component subunit beta, J. Mol. Biol. 427 (2015) 2104–2120.
[56] L. Tian, M. Neuber-Hess, J. Mewburn, et al., Ischemia-induced Drp1 and Fis1-mediated mitochondrial fission and right ventricular dysfunction in pulmonary hypertension, J. Mol. Med. (Berl.) 95 (2017) 381–393.
[57] J.S. Schlehe, M.S. Journel, K.P. Taylor, K.D. Amodeo, M.J. LaVoie, The mitochondrial disease associated protein Ndufaf2 is dispensable for Complex-1 assembly but critical for the regulation of oxidative stress, Neurobiol. Dis. 58 (2013) 57–67.
[58] L.D. Li, H.F. Sun, X.X. Liu, et al., Down-regulation of NDUFB9 promotes breast cancer cell proliferation, metastasis by mediating mitochondrial metabolism, PLoS One 10 (2015), e0144441.
[59] S. Caravita, C. Baratto, F. Di Marco, et al., Haemodynamic characteristics of COVID-19 patients with acute respiratory distress syndrome requiring mechanical ventilation. An invasive assessment using right heart catheterization, Eur. J. Heart Fail. 22 (2020) 2228–2237.
[60] M. Michaelis, M.C. Kleinschmidt, H.W. Doerr, J. Cinatl Jr., Minocycline inhibits West Nile virus replication and apoptosis in human neuronal cells, J. Antimicrob. Chemother. 60 (2007) 981–986.

[61] Z. Xu, Y. Zhang, Y. Cao, The roles of apoptosis in swine response to viral infection and pathogenesis of swine enteropathogenic coronaviruses, Front. Vet. Sci. 7 (2020), 572425.
[62] D. Bee, G.W. Gill, C.J. Emery, G.L. Salmon, T.W. Evans, G.R. Barer, Action of almitrine on the pulmonary vasculature in ferrets and rats, Bull. Eur. Physiopathol. Respir. 19 (1983) 539–545.
[63] E.K. Weir, I.F. McMurtry, A. Tucker, J.T. Reeves, R.F. Grover, Prostaglandin synthetase inhibitors do not decrease hypoxic pulmonary vasoconstriction, J. Appl. Physiol. 41 (1976) 714–718.
[64] S. Yokota, T. Miyamae, Y. Kuroiwa, K. Nishioka, Novel coronavirus disease 2019 (COVID-19) and cytokine storms for more effective treatments from an inflammatory pathophysiology, J. Clin. Med. 10 (2021) 801.